ORIGINAL PAPER

Phase relations and melting of carbonated peridotite between 10 and 20 GPa: a proxy for alkali- and CO$_2$-rich silicate melts in the deep mantle

Sujoy Ghosh · Konstantin Litasov · Eiji Ohtani

Abstract We determined the melting phase relations, melt compositions, and melting reactions of carbonated peridotite on two carbonate-bearing peridotite compositions (ACP: alkali-rich peridotite + 5.0 wt % CO$_2$ and PERC: fertile peridotite + 2.5 wt % CO$_2$) at 10–20 GPa and 1,500–2,100 °C and constrain isopleths of the CO$_2$ contents in the silicate melts in the deep mantle. At 10–20 GPa, near-solidus (ACP: 1,400–1,630 °C) carbonatitic melts with < 10 wt % SiO$_2$ and > 40 wt % CO$_2$ gradually change to carbonated silicate melts with > 25 wt % SiO$_2$ and < 25 wt % CO$_2$ between 1,480 and 1,670 °C in the presence of residual majorite garnet, olivine/wadsleyite, and clinoenstatite/clinopyroxene. With increasing degrees of melting, the melt composition changes to an alkali- and CO$_2$-rich silicate melt (Mg# = 83.7–91.6; ∼ 26–36 wt % MgO; ∼ 24–43 wt % SiO$_2$; ∼ 4–13 wt % CaO; ∼ 0.6–3.1 wt % Na$_2$O; and ∼ 0.5–3.2 wt % K$_2$O; ∼ 6.4–38.4 wt % CO$_2$). The temperature of the first appearance of CO$_2$-rich silicate melt at 10–20 GPa is ∼ 440–470 °C lower than the solidus of volatile-free peridotite. Garnet + wadsleyite + clinoenstatite + carbonatitic melt controls initial carbonated silicate melting at a pressure < 15 GPa, whereas garnet + wadsleyite/ringwoodite + carbonatitic melt dominates at pressure > 15 GPa. Similar to hydrous peridotite, majorite garnet is a liquidus phase in carbonated peridotites (ACP and PERC) at 10–20 GPa. The liquidus is likely to be at ∼ 2,050 °C or higher at pressures of the present study, which gives a melting interval of more than 670 °C in carbonated peridotite systems. Alkali-rich carbonated silicate melts may thus be produced through partial melting of carbonated peridotite to 20 GPa at near mantle adiabat or even at plume temperature. These alkali- and CO$_2$-rich silicate melts can percolate upward and may react with volatile-rich materials accumulate at the top of transition zone near 410-km depth. If these refertilized domains migrate upward and convect out of the zone of metal saturation, CO$_2$ and H$_2$O flux melting can take place and kimberlite parental magmas can be generated. These mechanisms might be important for mantle dynamics and are potentially effective metasomatic processes in the deep mantle.

Keywords Carbonated peridotite · Metasomatism · Partial melting · Experimental petrology · Kimberlite

Communicated by C. Ballhaus.

S. Ghosh · E. Ohtani
Department of Earth and Planetary Materials Science, Tohoku University, 6-3 Aoba, Aramaki, Aoba-ku, Sendai 980-8571, Japan

S. Ghosh (✉)
Institute of Geochemistry and Petrology, ETH Zürich, 8092 Zürich, Switzerland
e-mail: sujoy.ghosh@erdw.ethz.ch

K. Litasov
Novosibirsk State University, 630090 Novosibirsk, Russia

K. Litasov
V.S. Sobolev Institute of Geology and Mineralogy SB RAS, 630090 Novosibirsk, Russia

Introduction

Kimberlites are CO$_2$-rich alkaline ultrabasic magmas generally derived from a depth of 150–250 km (e.g., Dawson 1971; Eggler 1978; Eggler and Wendlandt 1979; Wyllie 1980; Mitchell 1995) and emplaced onto cratons (e.g., Haggerty 1999). These magmas are enriched in incompatible trace elements (e.g., Sr, Ba, Zr, Nb, and REE) and reflect multiple metasomatic processes in the lithospheric

mantle (Canil and Bellis 2007). Considerable debate remains on the origin of kimberlites regarding their depths of formation (e.g., Wyllie 1980; Ringwood et al. 1992; Mitchell 1995; Haggerty 1999; Hayman et al. 2005; Kaminsky et al. 2010), the composition of the source material—e.g., metasomatically enriched, previously melt-depleted, garnet peridotite facies lithospheric mantle or garnetite and clinopyroxenite and mica-rich veins (e.g., Foley 1992; Edgar and Charbonneau 1993; Tainton and McKenzie 1994; le Roex et al. 2003; Chalapathi Rao et al. 2004; Harris et al. 2004), and the concentrations of volatiles (H_2O, CO_2, F, Cl) in the primary magmas (e.g., Brey and Ryabchikov 1994; Brey et al. 2009; Foley et al. 2009; Litasov et al. 2010).

The global distribution of low-velocity regions in the Earth's mantle and transition zone (Forsyth et al. 1998; Tauzin et al. 2010; Schmerr 2012) provides evidence for large-scale occurrence of partial melting in the peridotite mantle. These anomalies (e.g., low shear wave velocity and high attenuation) can be explained by hydrous melting (Karato 2003), carbonated melting (Presnall and Gudfinnsson 2005), or by temperature variations (Stixrude and Lithgow-Bertelloni 2007). Electrical conductivity measurements also show several anomalies in the upper mantle and transition zone (Kelbert et al. 2009; Karato 2011; Naif et al. 2013), which can be interpreted as resulting from the presence of carbonate melts (Gaillard et al. 2008).

Petrological evidence based on inclusions in diamonds suggests that at oxidized conditions, carbonatitic melts could be present in the lower mantle (Walter et al. 2008, 2011). However, due to the small abundance of carbon in the mantle, i.e., $\sim$ 20–120 and 300–800 ppm C, respectively, for MORB and OIB source regions (Marty 2012), only a small fraction of carbonatitic melt could be generated in the deep upper mantle (Dasgupta and Hirschmann 2010) and such a small melt fraction should not change the physical properties (e.g., density and viscosity) of the mantle. This can be illustrated by the effect of solid carbonates on the density and velocity of the mantle peridotite or eclogite, which is negligible until the carbonate fraction is increased above 10 wt % (e.g., Litasov et al. 2008; Sanchez-Valle et al. 2011). Moreover, at depths greater than 150 km, the mantle is likely to be too reduced to host carbonates or carbonatite melts (Stagno and Frost 2010; Stagno et al. 2013). The mantle at depths greater than 250 km may be reduced enough to host an Fe,Ni metal phase (Frost et al. 2004; Rohrbach et al. 2007, 2011).

Previously, there were two different types of experiments conducted on carbonated peridotite at the upper mantle and transition zone depths. One type mainly focused on the near-solidus phase equilibria, where low-Si (less than 10 wt %) carbonatitic melts coexist with mantle assemblages (e.g., Dasgupta and Hirschmann 2006; Ghosh

et al. 2009; Rohrbach and Schmidt 2011). In the second set of experiment, the stability of carbonated silicate melts was constrained either in simplified systems (Gudfinnsson and Presnall 2005) or at a single pressure (Dalton and Presnall 1998a; Stagno and Frost 2010). Dasgupta et al. (2013) suggested that carbonated silicate melting can occur beneath the mid-ocean ridges down to 250 km depth. However, gradual change from carbonatite-to-silicate melt is still poorly constrained at $\geq$ 300 km depth, where redox melting probably starts (Rohrbach and Schmidt 2011).

In this study, we present phase relations, melt compositions, and melting reactions on two carbonated peridotite compositions, i.e., ACP: alkali-rich peridotite with 5 wt % CO_2 and PERC: fertile peridotite with 2.5 wt % CO_2, at pressures of 10–20 GPa (corresponding to the depths of 300 km and slightly shallower than 600 km) and temperatures of 1,500 to 2,100 °C. We also calculate isopleths of the CO_2 contents in the melts as a function of temperature. Finally, we discuss the gradual change of low-silica carboantitic melts to carbonated silicate melts dependent on pressure and temperature.

Experimental and analytical techniques

Starting materials

The starting materials were a synthetic alkali-rich carbonated peridotite (ACP) and carbonated fertile peridotite (PERC). They contained 5.0 and 2.5 wt % CO_2, respectively (Ghosh et al. 2009; Dasgupta and Hirschmann 2006) (Table 1). The starting materials were synthesized by heating the mixture of high-purity oxides and carbonates with the controlling oxygen fugacity. Carbon dioxide was added as $CaCO_3$, Na_2CO_3, K_2CO_3 (reagent grade carbonates), and natural magnesite, which contains 1.2 wt % FeO, 0.5 wt % MnO, and 0.3 wt % CaO; natural siderite, which contains 57.7 wt % FeO, 3.0 wt % MnO, and 0.2 wt % MgO according to the microprobe analyses. Oxides were mixed in an agate mortar under ethanol and then fired at 1,400 °C in a CO_2/H_2 gas mixing furnace under the controlled oxygen fugacity (fO_2) at log fO_2 = FMQ-1 to remove Fe^{+3} from the sample. The quenched sample of the mixture of glass and minerals (olivine, opx, cpx, garnet) with a peridotite composition was crushed and ground under ethanol for 60 min, after that carbonates were added, and finally, the entire mixture was mixed again under ethanol to homogenize the starting material.

Experimental procedure

All experiments were carried out in a 1,000-ton Kawai-type multi-anvil high-pressure apparatus at Tohoku University

Table 1 Compositions (wt %) of bulk starting materials used in this study, compared with the previous studies and pyrolite composition

	Pyrolite	KLB-1	PERC**	ACP**	SC1 + 10 % mst	HC	LC
SiO_2	45.20	44.54	42.29	42.40	40.86	43.40	36.30
TiO_2	0.70	0.21	0.20	0.30	0.17	0.01	0.15
Al_2O_3	3.50	3.70	3.52	4.20	3.69	2.51	3.25
Cr_2O_3	0.40	0.23	0.21	0.40	0.38	1.01	0.34
FeO*	8.00	8.08	8.07	7.60	6.92	6.57	6.14
MnO	0.10	0.14	0.13	–	0.12	0.10	0.10
MgO	37.50	39.30	39.26	35.60	38.62	39.20	34.9
NiO	0.20	–	–	–	0.20	0.17	0.18
CaO	3.10	3.52	3.52	3.60	3.47	0.81	3.09
Na_2O	0.60	0.29	0.29	0.50	0.34	0.02	0.30
K_2O	0.10	0.01	0.01	0.40	0.03	1.40	6.83
H_2O							
CO_2	–	–	2.51	5.00	5.22	4.80	8.40
Mg#	89.31	89.66	89.66	89.31	90.87	91.41	91.02
Ca#	5.04	5.46	5.46	6.09	5.55	1.34	5.47

Pyrolite model composition (Ringwood 1975)

KLB-1 is the composition of the fertile peridotite

Mg# = 100 × molar Mg/(Mg + Fe)

Ca# = 100 × molar Ca/(Ca + Mg + Fe)

SC1 + 10 % mst is the bulk composition used by Brey et al. (2008)

HC and LC are the bulk compositions used by Brey et al. (2011)

* Total Fe as FeO

** Starting material used in the present study

with the use of 26-mm edge length tungsten carbide cubes holding a 10 mm ZrO_2-octahedra within TEL of 3.5 mm (10/3.5 assembly). Furnace assembly was essentially the same as one used in Ghosh et al. (2009). A cylindrical straight lanthanum chromite ($LaCrO_3$) was used as a heating element. The starting material was packed into outer Pt and inner Re double capsules to avoid substantial Fe loss during the experiments. We have used the improved cell assembly in which the temperature gradient inside the cell is reduced by placing thick Re discs and foils inside Pt capsule (Ghosh et al. 2009). The temperature difference across the sample was found to be less than 50 °C in this cell assembly (Ghosh et al. 2009). Total capsule length was 1.4 mm. Pyrophyllite was used as a gasket material. To minimize the possibility of hydrogen diffusion from the gaskets, they were dried in the oven for at least 12 h at 230 °C. Other furnace assembly parts were fired in the oven for overnight at 800 °C to remove possible moisture from the assembly. Temperature was measured with $W_{97}Re_3$-$W_{75}Re_{25}$ C-type thermocouples with no correction for the effect of pressure on the emf. The uncertainty of the pressure measurements is considered to be ± 1 GPa (Litasov and Ohtani 2002).

The pressure calibrations at room temperature were carried out using semiconductor-to-metal transition in ZnS (15.6 GPa), GaAs (18.3 GPa), and GaP (22 GPa). At high temperature, pressure was calibrated based on the olivine–wadsleyite (14.3 GPa, 1,600 °C, Morishima et al. 1994) and wadsleyite–ringwoodite (17.4 GPa, 1,000 °C, Suzuki et al. 2000b) transitions. Load was applied to the assembly until the target pressure had been achieved and then temperature was raised at a rate of ∼ 50–100 °C/min.

Analytical methods

After each experiment, the recovered capsule was mounted into a low-viscosity epoxy resin and ground under petroleum benzine (Wako Co. Ltd.) to expose a cross section through the center of the sample. Water and other lubricants were avoided during polishing to preserve alkalis in the sample. The final surface of the run products was polished with dry diamond powder (1 and 3 μm in diameter). Finally, polished mounts were coated with a carbon film for electron microprobe analysis.

All experimental runs were analyzed by the wavelength dispersive electron microprobe analysis using a 5 spectrometer JEOL JXA-8200 electron microprobe at ETH Zürich. Electron beam conditions were set to 15 kV, 20 nA beam current for silicate minerals, counting times for Si, Ti, Cr, Al, Fe, Mg, and Ca were 20 s on peak and 10 s on

each background, and for Na and K were 10 s on peak and 5 s on each background. For carbonated silicate melts, counting times for all elements were 10 s on peak and 5 s on backgrounds. We used synthetic mineral standards of rutile (TiO_2) for Ti, corundum (Al_2O_3) for Al, periclase (MgO) for Mg, pyrolusite (MnO_2) for Mn and natural mineral standards of wollastonite ($CaSiO_3$) for Si and Ca, chromite $[(Mg,Fe)Cr_2O_4]$ for Cr, hematite (Fe_2O_3) for Fe, aegirine $[(Na,Fe)Si_2O_6]$ for Na, and K-feldspar ($KAlSi_3O_8$) for K. Raw data were corrected by the ZAF method. Quenched melt was analyzed using a defocused beam of 10–20 μm in diameter and reduced current of 5–10 nA to decrease the volatilization of

alkaline elements. Least-squares regression mass–balance calculations were performed on the bulk and phase compositions of ACP and PERC. For all experiments, CO_2 content of melts is calculated from difference between 100 and the measured analytical total from EPMA. Mass–balance calculations suggest that uncertainty is not more than 10 % in most of the experiments. Concentrations of alkalis (Na_2O and K_2O) in the melts were calculated by adding Na_2O and K_2O until the least-squares fit for these oxides were zero (Table 2).

Textural analysis of the sample was observed also using JEOL JSM-71010 field emission scanning electron microscope (FEG-SEM) operating with an acceleration voltage

Table 2 Summary of run conditions, phase assemblages, and calculated phase proportions

Run no.	P (GPa)	T (°C)	t (min)	Phase assemblage	ΔlogfO$_2$	Gt	Ol/Wd	Cen	csM	Na$_2$O-melt	K$_2$O-melt	Sum r^2
ACP (Peridotite + 5.0 wt % CO$_2$)												
D040	10.0	1,500	360	Gt, Ol, Cen, csM								
D013	10.0	1,600	360	Gt, Ol, Cen, csM	−2.90	32.0 (1.6)	24.3 (0.6)	27.7 (1.2)	16.1 (0.6)	3.10	3.15	0.44 (0.1)
D048	10.0	1,700	360	Gt, Ol, Cen, csM	−2.57	28.9 (0.8)	26.4 (0.5)	18.3 (0.8)	26.4 (2.1)	1.85	1.65	0.21 (0.1)
D003	10.0	1,800	240	Gt, Ol, csM		36.9 (0.3)	19.9 (0.6)		43.2 (2.2)	1.18	1.00	0.80 (0.1)
D055	10.0	1,900	15	Gt, csM		32.0			68.0	0.85	0.75	0.60
D052	10.0	2,000	60	Gt, csM		24.8 (1.0)			75.2 (0.1)	0.80	0.70	1.14 (0.1)
D049	12.5	1,700	480	Gt, Ol, Cen, csM	−2.94	36.8 (2.8)	24.9 (1.4)	22.9 (2.7)	15.4 (0.2)	2.38	2.30	0.57 (0.5)
D053	12.5	1,900	75	Gt, csM		25.0			75.0	0.85	0.75	1.30
D050	15.0	1,700	540	Gt, Wd, Cen, csM								
D008	15.0	1,825	60	Gt, Wd, Cen, csM	−2.64	43.6 (2.2)	27.5 (2.5)	3.0 (2.0)	25.9 (6.1)	1.28	1.25	0.80 (0.5)
D001	15.0	1,850	240	Gt, Wd, csM		47.4 (1.2)	25.2 (0.5)		27.4 (1.1)	1.10	1.00	0.60 (0.3)
D018	15.0	1,900	60	Gt, Wd, csM		40.0	22.0		38.0	1.10	1.00	0.33
D054	15.0	2,100	60	Gt, csM		15.0			85.0	0.85	0.75	0.76
D025	16.5	1,700	240	Gt, Wd, csM		53.5 (1.2)	28.2 (2.0)		18.3 (0.3)	2.65	2.93	0.21 (0.3)
D020	16.5	2,050	60	Gt, csM		48.7 (1.4)			51.3 (2.6)	1.18	1.15	0.99 (0.4)
D051	17.5	1,900	60	Gt, Wd, csM		19.7 (1.8)	31.0 (0.8)		49.3 (0.1)	0.80	0.75	0.05 (0.1)
D024	20.0	1,810	120	Gt, Wd, csM		51.3 (0.4)	25.8 (1.0)		23.0 (1.2)	1.45	1.52	1.11 (0.5)
D019	20.0	1,900	60	Gt, Wd, csM		47.4 (0.5)	25.1 (0.4)		27.5 (0.3)	1.52	1.50	0.38 (0.3)
D007	20.0	2,000	30	Gt, Wd, csM		38.6 (1.2)	19.2 (0.4)		42.2 (0.8)	1.00	0.95	0.16 (0.2)
D047	20.0	2,100	30	Gt, csM		35.3 (1.5)			64.7 (1.2)	0.57	0.50	0.62 (0.3)
PERC (Peridotite + 2.5 wt % CO$_2$)												
D057	10.0	1,800	240	Gt, Ol, Cpx, csM	−2.07	23.0	38.0	4.0	35.0	1.21	1.00	0.51
D056	10.0	2,000	30	csM								
D058	15.0	1,800	240	Gt, Wd, Cpx, csM								
D059	15.0	2,000	30	Gt, csM								
D060	20.0	1,800	240	Gt, Wd, csM		49.0	29.0		22.0	1.85	1.78	0.02
D061	20.0	2,000	60	Gt, Wd, Mw, csM		25.0	15.0		60.0	0.78	0.67	0.22

Phase proportions (in wt %) of all the phases were estimated by mass–balance calculation; the error are 1σ standard deviation with respect to mean for the calculated phase proportions, using uncertainties in analyzed phase compositions. "Sum r^2" is the summation of squares of residuals obtained by using mineral modes, phase compositions, and composition of starting material. Oxygen fugacity (fO_2) calculation is done by the estimated CO_2 mole fractions of carbonated silicate melt (Table 6), following the calibration of Stagno and Frost (2010). fO_2 values are reported as $\Delta logfO_2$ was calculated as $logfO_2$ (IW) − $logfO_2$ (experimental sample), where IW represents buffer set by the coexistence of iron and wüstite, and is used for calculation from O'Neill (1987)

Gt garnet, Ol olivine, Wd wadsleyite, Cen clinoenstatite, Cpx clinopyroxene, Mw magnesiowüstite, csM carbonated silicate melt

of 15 kV at Institute for Materials Research, Tohoku University.

Olivine and wadsleyite were also identified by Raman spectra of the polished samples using the JASCO NRS-2000 spectrometer with a nitrogen-cooled CCD detector at Tohoku University. A microscope was used to focus the excitation laser beam (514.5 nm lines of a Princeton Instruments Ar^+ laser).

Results

Twenty-six experiments were performed on two different bulk compositions (ACP and PERC; Table 1) at 10–20 GPa and 1,500–2,100 °C. A summary of run conditions, resulting phases, and calculated phase proportions are listed in Table 2. Backscattered electron images of representative charges are shown in Fig. 1a–f. Phase
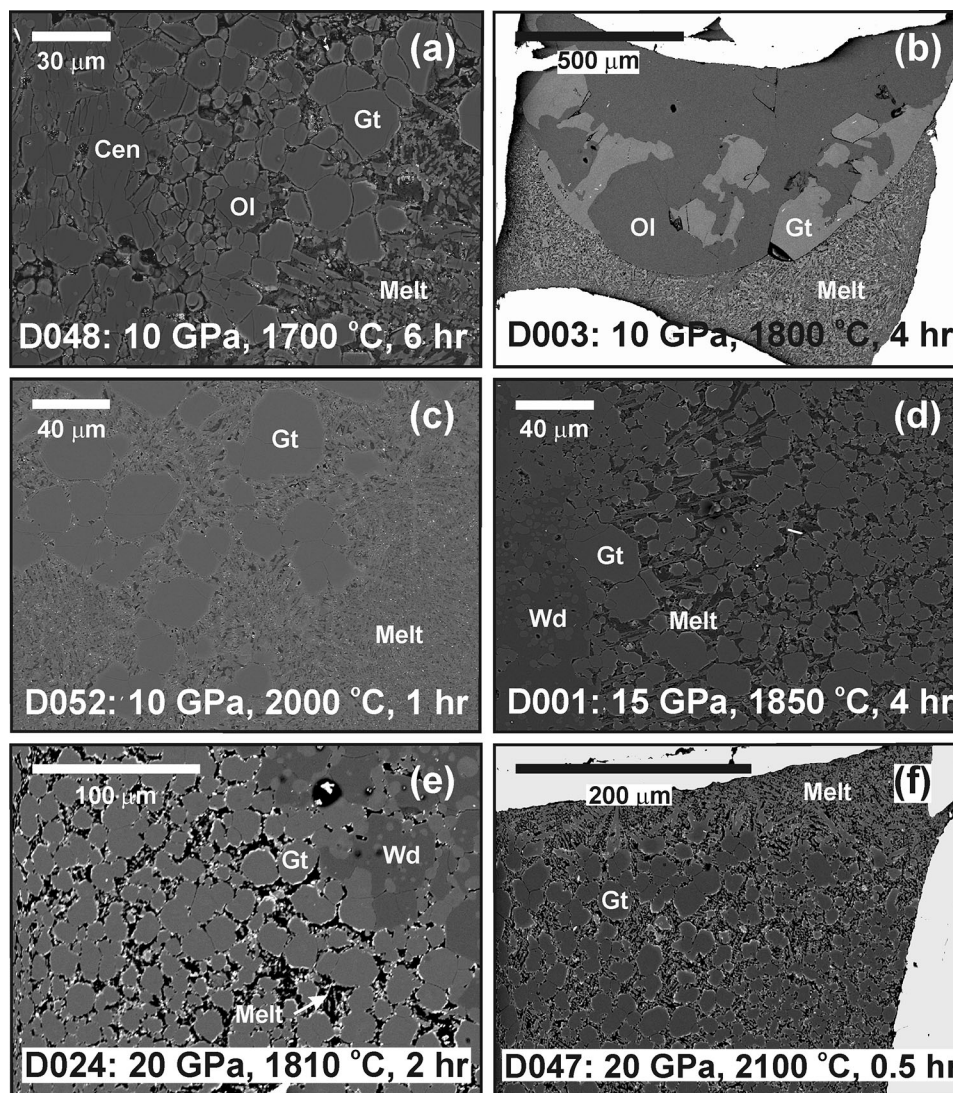

Fig. 1 Backscattered electron (BSE) images of run products in ACP bulk composition. *Gt* garnet, *Ol* olivine, *Wd* wadsleyite, *Cen* clinoenstatite, *Melt* carbonated silicate melt. **a** Run D048 (10 GPa, 1,700 °C, 6 h), quenched carbonated-rich silicate melt (*F*-26 %; Table 2) coexists with garnet, olivine, and clinoenstatite. **b** Run D003 (10 GPa, 1,800 °C, 4 h), a relatively large amount of quenched carbonated silicate melt (43 %) coexists with garnet and olivine. Melt is segregated to the hot side of the capsule and along the capsule wall. At similar pressure and temperature, the PERC bulk composition yields ca. 35 % of carbonated silicate melt coexisting with garnet, olivine, and clinopyroxene (run D057, not shown). **c** Run D052 (10 GPa, 2,000 °C, 1 h), quenched carbonated silicate melt coexists with rounded garnet. **d** Run D001 (15 GPa, 1,850 °C, 4 h), quenched melt is present at the grain edges of garnet and wadsleyite. Wadsleyites always contain rounded garnet inclusions, whereas at lower pressures, olivine crystals are inclusion-free. **e** Run D024 (20 GPa, 1,810 °C, 2 h), quenched carbonated silicate melt occurs along grains of garnet and wadsleyite. **f** Run D047 (20 GPa, 2,100 °C, 0.5 h), at relatively higher degree of melting (65 %), i.e., after exhaustion of wadsleyite, quenched melt is coexisting with garnet. In BSE images of melt-rich experiments, garnet grains show *thick white borders*. Majoritic garnet is the liquidus phase at 10–20 GPa in carbonated peridotite
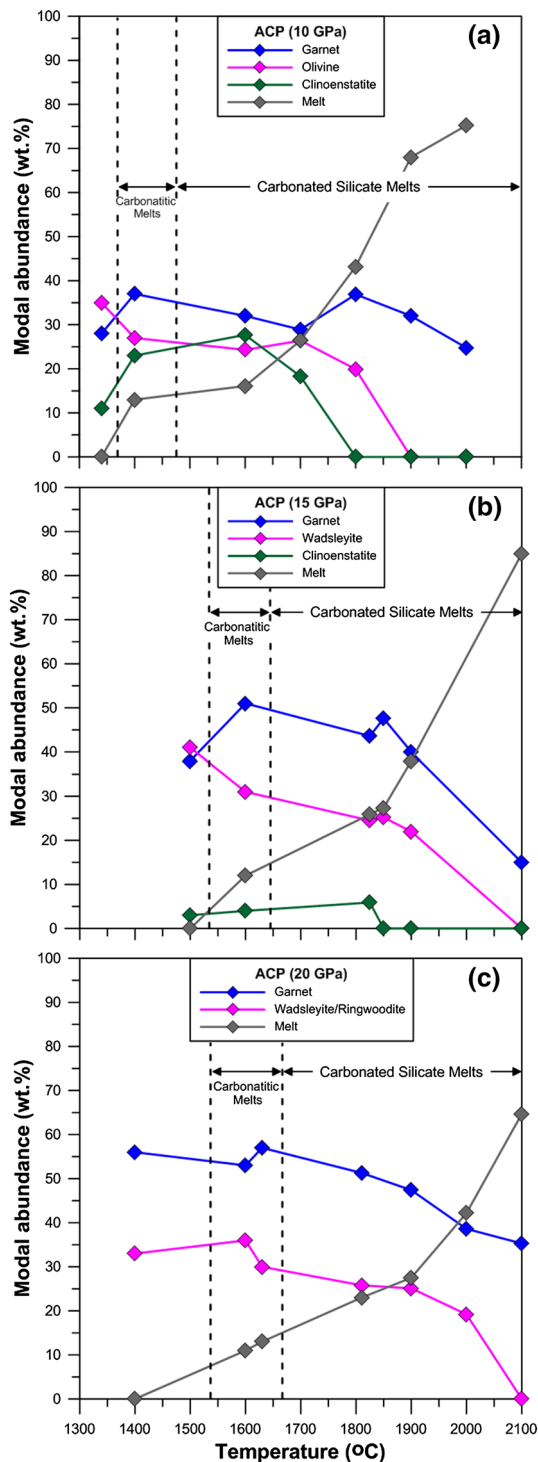
Fig. 2 Modal abundance (wt %) of majoritic garnet, olivine/wadsleyite, clinoenstatite, and carbonated silicate melt from mass–balance calculations of ACP **a** at 10 GPa, **b** 15 GPa, and **c** 20 GPa. The melts at ≤ 1,460 °C, ≤ 1,640 °C, and ≤ 1,670 °C for ACP are carbonatitic at 10, 15, and 20 GPa. With increasing temperature, a transition from carbonatitic-to-carbonated silicate melt is observed at 10–20 GPa in ACP

proportions estimated by mass–balance calculations are plotted in Fig. 2 as a function of temperature. Compositions of minerals and melts are given in Tables 3–6. Figure 3 shows phase relations in alkali-rich carbonated peridotite (ACP) to 20 GPa and solidi of carbonated peridotite in simple and complex systems to ∼ 660 km depth (Dalton and Presnall 1998b; Dasgupta and Hirschmann 2006; Ghosh et al. 2009; Rohrbach and Schmidt 2011). fO_2 is calculated only for those runs where olivine, clinoenstatite, and melt are present. As neither Graphite/diamond nor ReO_2 were found in any of the experiments, we suggest that fO_2 in the present study is at higher fO_2 than graphite–CO–CO_2 (CCO) but below the Re–ReO_2 (RRO) buffer. Oxygen fugacity, however, is likely to be at or close to the EMOD buffer because the coexisting phases have a strong buffering effect and also control the SiO_2 activity in the charges.

Phase relations

ACP bulk composition

Near-solidus phase relations at 10–20 GPa for ACP have been already reported in Ghosh et al. (2009). Clinopyroxene (hereafter Cpx) disappears just above the solidus at 10–15 GPa, which is located at lower temperatures compared to volatile-free peridotite (KLB-1: 15 GPa and 2,060 °C; Zhang and Herzberg 1994) and hydrous peridotite (CMAS: 10 GPa and 1,750 °C; Litasov and Ohtani 2002). The CO_2 content of the bulk decreases the stability field of Cpx, as observed in various studies on volatile-free and carbonated peridotites at low pressures (Hirose 1997; Walter 1998; Dasgupta et al. 2007b). Comparison with the hydrous system (Litasov and Ohtani 2002) indicates that CO_2 has a stronger effect to suppress Cpx stability than H_2O. Clinoenstatite (hereafter Cen), which has the ilmenite structure (Gasparik 2003), is stable to 1,700 °C at 12.5 GPa and 1,825 °C at 15 GPa, where it coexists with melt + garnet + olivine/wadsleyite. Experiments at higher temperature yield melt + garnet ± olivine/wadsleyite at these pressures. Cpx and Cen are stable to 15 GPa. Olivine/wadsleyite is stable to 1,800 °C at 10 GPa, 1,900 °C at 15 GPa, and 2,000 °C at 20 GPa. Garnet and melt are present in all experiments. Al_2O_3 contents in melts decrease with pressure, which is mainly due to increasing stability of garnet relative to olivine/wadsleyite. Similar to hydrous peridotite (Litasov and Ohtani 2002), majoritic garnet is the liquidus phase in carbonated peridotite at 10–20 GPa. Run products contain 25, 15, and 35 % (by mass–balance calculation) garnet coexisting with carbonated silicate melt at 2,000 °C and 10 GPa (D052), 2,100 °C and 15 GPa (D054), and 2,100 °C and 20 GPa (D047),

Table 3 Garnet composition

Run no.	D013		D048		D003		D055		D052		D049		D053		D050	
P (GPa)/T (°C)	10/1,600		10/1,700		10/1,800		10/1,900		10/2,000		12.5/1,700		12.5/1,900		15/1,700	
No. analyses	8		36		6		24		15		50		25		8	
SiO$_2$ (wt %)	46.44	(0.36)	47.15	(0.43)	47.62	(0.22)	47.77	(0.44)	47.18	(0.57)	48.65	(0.68)	48.09	(0.50)	51.46	(0.34)
TiO$_2$	0.42	(0.05)	0.21	(0.07)	0.15	(0.02)	0.09	(0.05)	0.08	(0.02)	0.37	(0.10)	0.08	(0.02)	0.42	(0.04)
Cr$_2$O$_3$	1.39	(0.05)	1.38	(0.13)	2.50	(0.16)	1.36	(0.06)	1.40	(0.04)	1.02	(0.23)	1.24	(0.04)	0.62	(0.08)
Al$_2$O$_3$	14.79	(0.83)	15.86	(0.50)	17.15	(0.47)	15.92	(0.62)	16.74	(0.34)	12.65	(1.00)	15.19	(0.42)	6.91	(0.50)
FeO^{tot}	5.20	(0.36)	5.28	(0.16)	1.22	(0.02)	3.49	(0.10)	3.06	(0.09)	6.63	(0.39)	3.19	(0.08)	7.33	(0.37)
MgO	27.78	(0.33)	27.76	(0.45)	29.29	(0.36)	29.78	(0.45)	29.33	(0.50)	28.38	(0.74)	29.94	(0.36)	28.05	(0.45)
CaO	2.97	(0.10)	2.01	(0.13)	1.70	(0.17)	1.47	(0.10)	1.15	(0.03)	2.42	(0.39)	1.34	(0.03)	4.76	(0.35)
Na$_2$O	0.17	(0.02)	0.10	(0.02)	0.07	(0.02)	0.08	(0.01)	0.09	(0.01)	0.17	(0.02)	0.11	(0.02)	0.45	(0.03)
K$_2$O	0.02	(0.01)	0.01	(0.01)	0.01	(0.00)	0.01	(0.01)	0.01	(0.00)	0.01	(0.01)	0.01	(0.01)	0.01	(0.01)
Sum	99.18		99.76		99.71		99.97		99.04		100.30		99.19		100.03	
Si^a (apfu)	3.243		3.273		3.268		3.274		3.260		3.372		3.317		3.600	
Ti	0.022		0.011		0.008		0.005		0.004		0.019		0.004		0.022	
Cr	0.077		0.076		0.136		0.074		0.076		0.056		0.068		0.035	
Al	1.217		1.298		1.387		1.286		1.364		1.033		1.235		0.570	
Fe^{tot}	0.304		0.306		0.070		0.200		0.177		0.384		0.184		0.429	
Mg	2.891		2.872		2.996		3.042		3.021		2.932		3.078		2.925	
Ca	0.222		0.149		0.125		0.108		0.085		0.180		0.099		0.357	
Na	0.023		0.013		0.009		0.011		0.012		0.023		0.015		0.061	
K	0.002		0.001		0.001		0.001		0.001		0.001		0.001		0.001	
Sum	8.000		8.000		8.000		8.000		8.000		8.000		8.000		8.000	
Mg#	90.50		90.36		97.72		93.83		94.47		88.41		94.36		87.21	
Ca#	6.50		4.49		3.92		3.22		2.59		5.14		2.95		9.62	
Majorite (mol %)	0.24		0.27		0.27		0.27		0.26		0.37		0.32		0.60	
Pyrope (mol %)	0.53		0.56		0.59		0.59		0.62		0.44		0.56		0.19	
Run no.	D008		D001		D018		D054		D025		D020		D051		D024	
P (GPa)/T (°C)	15/1,825		15/1,850		15/1,900		15/2,100		16.5/1,700		16.5/2,050		17.5/1,900		20/1,810	
No. analyses	4		13		5		17		6		3		13		9	
SiO$_2$ (wt %)	51.76	(0.38)	51.74	(0.83)	51.65	(0.63)	51.56	(0.68)	52.43	(0.59)	53.21	(0.24)	51.38	(0.35)	53.61	(0.40)
TiO$_2$	0.23	(0.05)	0.28	(0.06)	0.14	(0.03)	0.13	(0.07)	0.36	(0.04)	0.15	(0.02)	0.24	(0.05)	0.16	(0.01)
Cr$_2$O$_3$	0.66	(0.13)	0.61	(0.10)	0.79	(0.02)	0.81	(0.11)	0.65	(0.09)	0.72	(0.03)	0.64	(0.10)	0.61	(0.06)
Al$_2$O$_3$	8.95	(0.44)	8.13	(0.71)	9.02	(0.33)	10.19	(0.54)	6.70	(0.93)	8.38	(0.21)	8.32	(0.81)	7.15	(0.39)
FeO^{tot}	4.79	(0.32)	5.88	(0.20)	4.38	(0.10)	3.93	(0.21)	6.42	(0.15)	4.67	(0.04)	5.50	(0.18)	5.19	(0.14)
MgO	31.45	(0.54)	30.52	(0.48)	31.89	(0.24)	32.58	(0.55)	29.77	(0.80)	30.75	(0.24)	30.45	(0.50)	30.69	(0.58)
CaO	2.04	(0.18)	2.14	(0.30)	1.80	(0.07)	1.62	(0.12)	2.94	(0.55)	1.67	(0.11)	2.67	(0.50)	2.22	(0.09)
Na$_2$O	0.20	(0.03)	0.18	(0.04)	0.18	(0.01)	0.12	(0.02)	0.26	(0.02)	0.16	(0.01)	0.24	(0.02)	0.23	(0.02)
K$_2$O	0.02	(0.01)	0.01	(0.01)	0.11	(0.04)	0.01	(0.01)	0.04	(0.03)	0.02	(0.02)	0.01	(0.01)	0.02	(0.01)
Sum	100.10		99.49		99.96		100.95		99.57		99.73		99.45		99.88	
Si^a (apfu)	3.555		3.597		3.543		3.492		3.661		3.681		3.568		3.711	
Ti	0.012		0.015		0.007		0.007		0.019		0.008		0.013		0.008	
Cr	0.036		0.034		0.043		0.043		0.036		0.039		0.035		0.033	
Al	0.725		0.666		0.729		0.813		0.552		0.683		0.681		0.583	
Fe^{tot}	0.275		0.342		0.251		0.223		0.375		0.270		0.319		0.300	
Mg	3.219		3.162		3.260		3.288		3.099		3.171		3.152		3.166	
Ca	0.150		0.159		0.132		0.118		0.220		0.124		0.199		0.165	
Na	0.026		0.024		0.024		0.016		0.035		0.021		0.032		0.031	
K	0.001		0.001		0.010		0.001		0.004		0.002		0.001		0.002	
Sum	8.000		8.000		8.000		8.000		8.000		8.000		8.000		8.000	
Mg#	92.13		90.25		92.85		93.66		89.21		92.15		90.80		91.34	

Table 3 continued

Run no.	D008	D001	D018	D054	D025	D020	D051	D024
P (GPa)/T (°C)	15/1,825	15/1,850	15/1,900	15/2,100	16.5/1,700	16.5/2,050	17.5/1,900	20/1,810
No. analyses	4	13	5	17	6	3	13	9
Ca#	4.13	4.35	3.63	3.24	5.95	3.47	5.41	4.53
Majorite (mol %)	0.55	0.60	0.54	0.49	0.66	0.68	0.57	0.71
Pyrope (mol %)	0.31	0.28	0.31	0.37	0.21	0.23	0.28	0.21

Run no.	D019		D007		D047		D057		D060		D061	
P (GPa)/T (°C)	20/1,900		20/2,000		20/2,100		10/1,800		15/1,800		20/2,000	
No. analyses	19		8		11		25		49		35	
SiO_2 (wt %)	52.85	(0.51)	52.44	(0.63)	51.00	(0.69)	47.34	(0.52)	51.67	(0.71)	52.02	(1.29)
TiO_2	0.15	(0.05)	0.10	(0.02)	0.07	(0.04)	0.24	(0.05)	0.20	(0.02)	0.09	(0.05)
Cr_2O_3	0.63	(0.09)	0.70	(0.03)	1.15	(0.08)	0.70	(0.09)	0.36	(0.07)	0.36	(0.22)
Al_2O_3	7.74	(0.81)	8.26	(0.67)	12.00	(2.13)	14.70	(0.72)	8.35	(0.75)	8.80	(1.05)
FeO^{tot}	5.17	(0.24)	4.11	(0.28)	2.26	(0.56)	6.39	(0.43)	5.61	(0.23)	3.95	(0.38)
MgO	31.74	(0.53)	32.09	(0.48)	30.89	(0.49)	26.14	(0.57)	29.32	(0.78)	30.87	(1.05)
CaO	1.82	(0.28)	2.27	(0.09)	1.89	(0.30)	3.64	(0.36)	4.28	(0.36)	2.92	(0.85)
Na_2O	0.19	(0.02)	0.21	(0.02)	0.20	(0.04)	0.10	(0.02)	0.14	(0.02)	0.10	(0.01)
K_2O	0.01	(0.00)	0.01	(0.01)	0.01	(0.00)	0.01	(0.01)	0.01	(0.00)	0.01	(0.00)
Sum	100.30		100.19		99.47		99.26		99.94		99.12	
Si^a (apfu)	3.628		3.588		3.503		3.328		3.588		3.606	
Ti	0.008		0.005		0.004		0.013		0.010		0.005	
Cr	0.034		0.038		0.062		0.039		0.020		0.020	
Al	0.626		0.666		0.972		1.218		0.683		0.719	
Fe^{tot}	0.297		0.235		0.130		0.376		0.326		0.229	
Mg	3.247		3.273		3.163		2.739		3.035		3.190	
Ca	0.134		0.166		0.139		0.274		0.318		0.217	
Na	0.025		0.028		0.027		0.014		0.019		0.013	
K	0.001		0.001		0.001		0.001		0.001		0.001	
Sum	8.000		8.000		8.000		8.000		8.000		8.000	
Mg#	91.63		93.30		96.06		87.94		90.31		93.30	
Ca#	3.64		4.53		4.05		8.09		8.65		5.96	
Majorite (mol %)	0.63		0.59		0.50		0.33		0.59		0.61	
Pyrope (mol %)	0.26		0.28		0.40		0.50		0.28		0.31	

Numbers in parentheses are one standard deviation

[a] Cations calculated on the basis of 8 cations and 12 oxygens

respectively. The liquidus temperature of the carbonated peridotite is close to hydrous peridotite (Litasov and Ohtani 2002), but may be slightly lower than of an volatile-free peridotite (Zhang and Herzberg 1994) at 10–20 GPa, which gives more than 670 °C melting interval in the carbonated system.

PERC bulk composition

The experimental interval of ∼ 200 °C does not allow us to constrain the phase relations in this composition. Although we observe Cpx is stable to 1,800 °C at 10–15 GPa, where it coexists with melt + garnet + olivine/wadsleyite, experiments at higher temperature yield melt ± garnet at these pressures. At 20 GPa, melt coexists with garnet + wadsleyite ± magnesiowüstite to 2,000 °C. Magnesiowüstite has been found only at 2,000 °C and 20 GPa with Mg# of 89.2. Carbonated silicate melts is stable at 2,000 °C and 20 GPa. Similar to ACP bulk composition, majoritic garnet is liquidus phase over the investigated pressure range.

Table 4 Olivine/wadsleyite composition

Run no.	D013		D048		D003		D049		D008		D001		D018		D025	
P (GPa) /T (°C)	10/1,600		10/1,700		10/1,800		12.5/1,700		15 /1,825		15/1,850		15 /1,900		16.5/1,700	
No. analyses	8		36		6		50		7		13		3		21	
SiO_2 (wt %)	40.74	(0.26)	41.58	(0.14)	42.92	(0.19)	41.47	(0.18)	41.18	(0.65)	41.30	(0.46)	40.89	(0.16)	41.54	(0.20)
TiO2	0.02	(0.00)	0.01	(0.01)	0.01	(0.01)	0.02	(0.02)	0.05	(0.02)	0.01	(0.01)	0.02	(0.01)	0.04	(0.02)
Cr_2O_3	0.05	(0.03)	0.07	(0.03)	0.14	(0.03)	0.04	(0.03)	0.13	(0.05)	0.04	(0.03)	0.11	(0.06)	0.10	(0.02)
Al_2O_3	0.02	(0.02)	0.05	(0.02)	0.10	(0.02)	0.06	(0.06)	0.24	(0.05)	0.06	(0.03)	0.42	(0.02)	0.19	(0.06)
FeO^{tot}	5.23	(0.11)	5.45	(0.09)	1.40	(0.17)	6.58	(0.10)	7.11	(0.16)	6.20	(0.09)	6.52	(0.11)	8.98	(0.14)
MgO	53.35	(0.52)	52.73	(0.37)	55.45	(0.22)	52.59	(0.49)	50.71	(0.70)	52.17	(0.27)	51.38	(0.32)	50.31	(0.38)
CaO	0.07	(0.01)	0.06	(0.02)	0.07	(0.01)	0.07	(0.05)	0.03	(0.02)	0.09	(0.02)	0.03	(0.01)	0.03	(0.03)
Na_2O	0.07	(0.02)	0.05	(0.03)	0.04	(0.01)	0.05	(0.02)	0.06	(0.04)	0.04	(0.02)	0.10	(0.02)	0.07	(0.02)
K_2O	0.02	(0.01)	0.01	(0.01)	0.00	(0.00)	0.01	(0.01)	0.02	(0.00)	0.01	(0.01)	0.09	(0.04)	0.01	(0.01)
Sum	99.57		100.01		100.13		100.89		99.53		99.92		99.56		101.27	
Si^a (apfu)	0.978		0.998		1.013		0.990		1.002		0.995		0.990		1.001	
Ti	0.000		0.000		0.000		0.000		0.001		0.000		0.000		0.001	
Cr	0.001		0.001		0.003		0.001		0.003		0.001		0.002		0.002	
Al	0.001		0.001		0.003		0.002		0.007		0.002		0.012		0.005	
Fe^{tot}	0.105		0.109		0.028		0.131		0.145		0.125		0.132		0.181	
Mg	1.909		1.886		1.950		1.871		1.839		1.873		1.855		1.806	
Ca	0.002		0.002		0.002		0.002		0.001		0.002		0.001		0.001	
Na	0.003		0.002		0.002		0.002		0.003		0.002		0.005		0.003	
K	0.001		0.000		0.000		0.000		0.001		0.000		0.003		0.000	
Sum	3.000		3.000		3.000		3.000		3.001		3.000		3.000		3.000	
Mg#	94.79		94.52		98.60		93.44		92.71		93.75		93.35		90.90	

Run no.	D051		D024		D019		D007		D057		D060		D061	
P (GPa)/T (°C)	17.5/1,900		20/1,810		20/1,900		20/2,000		10/1,800		20/1,800		20/2,000	
No. analyses	18		5		20		4		79		48		12	
SiO_2 (wt %)	40.73	(0.39)	41.78	(0.13)	41.08	(0.49)	41.24	(0.53)	41.39	(0.42)	41.05	(0.47)	41.42	(0.20)
TiO_2	0.04	(0.02)	0.05	(0.02)	0.04	(0.02)	0.01	(0.01)	0.02	(0.01)	0.03	(0.02)	0.02	(0.01)
Cr_2O_3	0.14	(0.03)	0.14	(0.02)	0.17	(0.03)	0.19	(0.03)	0.03	(0.02)	0.08	(0.03)	0.09	(0.02)
Al_2O_3	0.42	(0.21)	0.31	(0.02)	0.47	(0.12)	0.59	(0.24)	0.08	(0.10)	0.42	(0.08)	0.68	(0.04)
FeO^{tot}	7.77	(0.13)	7.31	(0.17)	7.38	(0.19)	6.69	(0.11)	6.78	(0.24)	7.70	(0.14)	5.96	(0.17)
MgO	50.99	(0.93)	49.67	(0.38)	50.76	(0.78)	51.66	(0.91)	51.20	(0.67)	51.00	(0.52)	52.23	(0.41)
CaO	0.07	(0.12)	0.02	(0.01)	0.03	(0.04)	0.07	(0.07)	0.15	(0.02)	0.04	(0.04)	0.03	(0.01)
Na_2O	0.11	(0.02)	0.09	(0.02)	0.09	(0.02)	0.09	(0.04)	0.06	(0.02)	0.08	(0.01)	0.06	(0.01)
K_2O	0.01	(0.01)	0.02	(0.01)	0.01	(0.00)	0.02	(0.01)	0.01	(0.00)	0.01	(0.00)	0.01	(0.01)
Sum	100.28		99.39		100.03		100.56		99.72		100.41		100.5	
Si^a (apfu)	0.984		1.022		0.995		0.990		1.003		0.991		0.992	
Ti	0.001		0.001		0.001		0.000		0.000		0.001		0.000	
Cr	0.003		0.003		0.003		0.004		0.001		0.002		0.002	
Al	0.012		0.009		0.013		0.017		0.002		0.012		0.019	
Fe^{tot}	0.157		0.150		0.149		0.134		0.137		0.155		0.119	
Mg	1.836		1.811		1.833		1.849		1.849		1.835		1.864	
Ca	0.002		0.001		0.001		0.002		0.004		0.001		0.001	
Na	0.005		0.004		0.004		0.004		0.003		0.004		0.003	
K	0.000		0.001		0.000		0.001		0.000		0.000		0.000	
Sum	3.000		3.000		3.000		3.000		3.000		3.000		3.000	
Mg#	92.12		92.37		92.46		93.23		93.09		92.19		93.98	

Numbers in parentheses are one standard deviation

[a] Cations calculated on the basis of 3 cations and 4 oxygens

Approach to equilibrium

We could not observe any compositional zoning in silicate phases. Although in lower temperature runs at subsolidus conditions (Ghosh et al. 2009), garnet shows compositional zoning (patchy Fe–Mg zones or Fe-rich cores with Mg-rich rims). All phases are compositionally homogeneous throughout the capsule. Generally, well-crystallized grains with equilibrium grain boundaries indicate textural equilibrium (Fig. 1). The compositions of all minerals and melts show systematic trends of variation with the pressure and temperature. Phase proportions were calculated from mass balance (Fig. 2) also suggest that the present experiments are close to equilibrium. Mass–balance calculation suggests FeO_{tot} loss is less than 3–8 wt %, relative to the bulk FeO_{tot} content in most of the experiments.

Mineral compositions

The compositions of six phases are measured in these experiments—carbonated silicate melt, majoritic garnet, olivine/wadsleyite, and clinoenstatite/cpx—as a function of temperature between 10 and 20 GPa for ACP and PERC.

Garnet–garnets appear as idiomorphic and 10–40 μm large crystals. In runs at 1,850 and 2,100 °C, close to its upper stability limit, more rounded garnet crystals form (Fig. 1c, d). They are free from inclusions and compositionally unzoned. Garnet contains 6.7–16.7 wt % Al_2O_3, 1.2–4.8 wt % CaO, 0.1–0.4 wt % TiO_2, 0.4–1.4 wt % Cr_2O_3, and 0.1–0.5 wt % Na_2O. Al_2O_3 content increases with temperature at 15–20 GPa, whereas CaO content decreases with increasing temperature at 10–20 GPa (Fig. 4). Majorite component (mol %) in garnet is in the range of 24–71 at 10–20 GPa.

The number of Si (pfu) is increased from 3.24 to 3.27 at 10 GPa and from 3.50 to 3.71 at 20 GPa, respectively (Fig. 5a; Table 3). The strong positive correlation between Si and pressure is in agreement with the previous data on volatile-free peridotite (Akaogi and Akimoto 1979; Irifune 1987; Ito and Takahashi 1987; Suzuki et al. 2000a; Walter 1998, Corgne et al. 2012), hydrous peridotite (Kawamoto et al. 1995; Kawamoto 2004), and carbonated peridotite (this study; Rohrbach and Schmidt 2011).

The sum of Al and Cr (pfu) is decreased from 1.3 to 1.5 at 10 GPa and 0.6–0.7 at 20 GPa, respectively (Fig. 5b). At same pressure, Si (pfu) and Al + Cr (pfu) in garnet do not change much with increasing temperature in volatile-free, hydrous and carbonated peridotite to 20 GPa.

The Mg number (Mg# = $100 \times$ molar Mg/[Mg + Fe^{tot}]) of majoritic garnet is increasing slightly with

Table 5 Clinoenstatite composition

Run no.	D013		D048		D049		D008		D057[a]	
P (GPa)/T (°C)	10/1,600		10/1,700		12.5/1,700		15/1,825		10/1,800	
No. analyses	3		23		79		3		26	
SiO_2 (wt %)	57.68	(0.13)	58.08	(0.45)	58.24	(0.44)	59.10	(0.46)	56.42	(0.64)
TiO_2	0.03	(0.03)	0.02	(0.01)	0.02	(0.02)	0.05	(0.00)	0.03	(0.01)
Cr_2O_3	0.07	(0.03)	0.08	(0.02)	0.07	(0.03)	0.04	(0.01)	0.10	(0.03)
Al_2O_3	0.25	(0.02)	0.33	(0.04)	0.25	(0.08)	0.12	(0.02)	1.11	(0.04)
FeO^{tot}	3.32	(0.32)	3.14	(0.17)	3.67	(0.26)	2.46	(0.02)	4.16	(0.08)
MgO	36.71	(0.50)	37.02	(0.41)	37.02	(0.49)	38.12	(0.05)	25.97	(0.57)
CaO	0.62	(0.05)	0.42	(0.03)	0.62	(0.19)	0.45	(0.02)	10.79	(0.67)
Na_2O	0.13	(0.01)	0.07	(0.02)	0.11	(0.02)	0.09	(0.01)	0.75	(0.03)
K_2O	0.01	(0.01)	0.01	(0.01)	0.01	(0.01)	0.02	(0.01)	0.01	(0.01)
Sum	98.82		99.17		100.01		100.45		99.34	
Si^{b} (apfu)	1.981		1.987		1.979		1.989		1.996	
Ti	0.001		0.001		0.001		0.001		0.001	
Cr	0.002		0.002		0.002		0.001		0.003	
Al	0.010		0.013		0.010		0.005		0.046	
Fe^{tot}	0.095		0.090		0.104		0.069		0.123	
Mg	1.879		1.887		1.875		1.912		1.370	
Ca	0.023		0.015		0.023		0.016		0.409	
Na	0.009		0.005		0.007		0.006		0.051	
K	0.000		0.000		0.000		0.001		0.000	
Sum	4.000		4.000		4.000		4.000		4.000	
Mg#	95.17		95.46		94.73		96.51		91.76	
Ca#	1.14		0.77		1.13		0.81		21.51	

Numbers in parentheses are one standard deviation

[a] Cpx produced from the bulk PERC composition

[b] Cations calculated on the basis of 4 cations and 6 oxygens

Table 6 Carbonated silicate melt composition

Run no.	D013		D048		D003		D055		D052		D049		D053	
P (GPa) /T (°C)	10/1,600		10/1,700		10/1,800		10/1,900		10/2,000		12.5/1,700		12.5/1,900	
No. analyses	4		15		23		29		15		14		16	
SiO_2 (wt %)	17.79	(0.74)	26.70	(2.41)	35.28	(1.07)	39.47	(1.77)	40.61	(0.89)	14.99	(0.86)	39.73	(1.23)
TiO_2	0.78	(0.10)	0.53	(0.08)	0.51	(0.03)	0.29	(0.08)	0.31	(0.06)	0.72	(0.13)	0.29	(0.09)
Cr_2O_3	0.05	(0.01)	0.12	(0.06)	0.32	(0.02)	0.38	(0.09)	0.40	(0.16)	0.08	(0.06)	0.29	(0.09)
Al_2O_3	0.50	(0.02)	1.13	(0.25)	1.02	(0.06)	3.01	(0.29)	2.95	(0.18)	0.28	(0.07)	2.18	(0.14)
FeO^{tot}	6.51	(0.50)	8.48	(0.56)	2.51	(0.09)	7.62	(0.45)	7.04	(0.28)	7.42	(0.59)	7.56	(0.40)
MgO	26.46	(1.37)	28.07	(3.23)	34.32	(0.85)	31.81	(2.01)	33.62	(0.45)	27.53	(2.82)	33.73	(0.86)
CaO	12.90	(0.87)	8.76	(1.80)	6.78	(0.32)	3.93	(0.38)	3.78	(0.17)	12.04	(2.37)	4.18	(0.25)
Na_2O	2.14	(0.30)	1.00	(0.22)	1.08	(0.11)	1.09	(0.11)	1.21	(0.16)	2.38	(1.00)	1.22	(0.10)
K_2O	0.32	(0.03)	0.13	(0.02)	0.55	(0.08)	0.42	(0.06)	0.37	(0.07)	0.57	(0.18)	0.18	(0.06)
CO_2*	32.55	(1.34)	25.08	(2.97)	17.63	(0.96)	11.98	(3.24)	9.71	(1.27)	33.99	(1.59)	10.64	(1.50)
$CO_2^{\#}$	40.60		20.95		12.70		9.20		9.20		29.55		9.20	
Si^a (apfu)	1.442		1.846		2.084		2.186		2.183		1.270		2.170	
Ti	0.048		0.028		0.023		0.012		0.013		0.046		0.012	
Cr	0.003		0.007		0.015		0.017		0.017		0.005		0.013	
Al	0.048		0.092		0.071		0.196		0.187		0.028		0.140	
Fe^{tot}	0.441		0.490		0.124		0.353		0.316		0.525		0.345	
Mg	3.197		2.893		3.022		2.625		2.693		3.475		2.746	
Ca	1.120		0.649		0.429		0.233		0.218		1.092		0.245	
Na	0.336		0.134		0.124		0.117		0.126		0.391		0.129	
K	0.033		0.011		0.041		0.030		0.025		0.062		0.013	
Mg#	87.87		85.51		96.06		88.15		89.49		86.87		88.83	
Ca#	23.54		16.09		12.00		7.26		6.74		21.45		7.33	

Run no.	D008		D001		D018		D054		D025		D020		D051	
P (GPa)/T (°C)	15/1,825		15/1,850		15/1,900		15/2,100		16.5/1,700		16.5/2,050		17.5/1,900	
No. analyses	4		4		7		7		7		8		12	
SiO_2 (wt %)	31.91	(2.30)	29.27	(0.73)	35.12	(0.89)	38.52	(1.91)	14.30	(2.02)	34.21	(2.17)	42.15	(1.77)
TiO_2	0.42	(0.06)	0.50	(0.06)	0.42	(0.05)	0.44	(0.12)	0.23	(0.24)	0.27	(0.09)	0.36	(0.10)
Cr_2O_3	0.05	(0.02)	0.06	(0.02)	0.11	(0.03)	0.21	(0.06)	0.10	(0.07)	0.09	(0.06)	0.56	(0.14)
Al_2O_3	0.41	(0.10)	0.62	(0.09)	0.93	(0.04)	1.26	(0.09)	1.11	(0.50)	0.72	(0.35)	5.25	(0.42)
FeO^{tot}	8.34	(1.09)	10.30	(0.44)	8.71	(0.14)	8.44	(1.27)	5.58	(1.02)	9.28	(0.92)	6.87	(0.38)
MgO	31.01	(1.23)	30.77	(0.96)	31.44	(0.42)	34.63	(2.71)	34.17	(2.84)	34.19	(2.00)	29.71	(0.73)
CaO	8.15	(1.11)	7.37	(0.27)	5.70	(0.28)	5.02	(1.35)	5.68	(2.07)	4.59	(0.74)	3.88	(0.33)
Na_2O	0.82	(0.03)	0.64	(0.04)	0.75	(0.06)	0.69	(0.22)	0.26	(0.13)	0.86	(0.17)	0.32	(0.07)
K_2O	0.10	(0.02)	0.08	(0.06)	0.19	(0.02)	0.06	(0.04)	0.13	(0.07)	0.35	(0.22)	0.08	(0.04)
CO_2*	18.79	(3.51)	20.39	(0.95)	16.63	(1.16)	10.73	(2.18)	38.44	(2.77)	15.44	(2.45)	10.82	(1.78)
$CO_2^{\#}$	29.50		13.70		12.70		9.20		38.44		14.90		9.32	
Si^a (apfu)	1.994		1.896		2.101		2.126		1.230		2.029		2.258	
Ti	0.020		0.024		0.019		0.018		0.015		0.012		0.015	
Cr	0.002		0.003		0.005		0.009		0.007		0.004		0.024	
Al	0.030		0.047		0.066		0.082		0.112		0.050		0.332	
Fe^{tot}	0.436		0.558		0.436		0.390		0.401		0.460		0.308	
Mg	2.888		2.971		2.803		2.849		4.379		3.022		2.372	
Ca	0.546		0.511		0.365		0.297		0.523		0.292		0.223	
Na	0.099		0.080		0.087		0.074		0.043		0.099		0.033	
K	0.008		0.007		0.014		0.004		0.014		0.026		0.005	
Mg#	86.89		84.19		86.55		87.97		91.61		86.79		88.52	
Ca#	14.10		12.66		10.13		8.40		9.86		7.73		7.67	

Table 6 continued

Run no.	D024		D019		D007		D047		D057		D060		D061	
P (GPa)/T (°C)	20/1810		20/1900		20/2000		20/2100		10/1800		20/1,800		20/2,000	
No. analyses	9		7		15		12		7		27		16	
SiO_2 (wt %)	23.80	(2.90)	30.48	(1.76)	35.63	(2.07)	42.90	(1.95)	37.77	(1.24)	24.00	(2.00)	38.94	(0.79)
TiO_2	0.23	(0.10)	0.44	(0.27)	0.46	(0.07)	0.26	(0.10)	0.70	(0.12)	0.59	(0.27)	0.37	(0.10)
Cr_2O_3	0.11	(0.02)	0.21	(0.07)	0.19	(0.08)	0.67	(0.14)	0.08	(0.04)	0.08	(0.05)	0.18	(0.07)
Al_2O_3	0.12	(0.05)	0.91	(0.23)	1.48	(0.22)	4.11	(1.06)	1.58	(0.15)	0.41	(0.08)	1.67	(0.09)
FeO^{tot}	11.17	(1.02)	10.30	(0.28)	9.71	(0.84)	6.81	(0.85)	11.28	(1.08)	9.56	(0.79)	10.06	(0.33)
MgO	32.25	(2.74)	34.55	(1.38)	33.05	(1.29)	35.56	(2.25)	25.61	(2.34)	29.68	(2.04)	33.64	(1.02)
CaO	7.14	(1.52)	4.37	(0.75)	6.53	(0.79)	2.98	(0.50)	9.18	(1.50)	11.26	(1.74)	5.73	(0.42)
Na_2O	1.57	(0.36)	0.79	(0.20)	0.37	(0.08)	0.28	(0.08)	1.21	(0.25)	1.33	(0.54)	0.34	(0.12)
K_2O	0.34	(0.08)	0.15	(0.04)	0.03	(0.02)	0.07	(0.04)	0.08	(0.02)	0.12	(0.06)	0.02	(0.02
CO_2*	23.27	(4.04)	17.80	(1.09)	12.55	(1.45)	6.36	(1.11)	12.51	(1.25)	22.97	(2.41)	9.05	(1.34)
$CO_2^{\#}$	20.00		20.00		11.14		6.20		14.00		22.54		8.45	
Si^a (apfu)	1.654		1.888		2.043		2.194		2.187		1.664		2.124	
Ti	0.012		0.020		0.020		0.010		0.030		0.031		0.015	
Cr	0.006		0.010		0.009		0.027		0.004		0.004		0.008	
Al	0.010		0.066		0.100		0.248		0.108		0.034		0.107	
Fe^{tot}	0.649		0.534		0.465		0.291		0.546		0.554		0.459	
Mg	3.341		3.190		2.824		2.710		2.210		3.068		2.735	
Ca	0.532		0.290		0.401		0.163		0.570		0.837		0.335	
Na	0.212		0.095		0.041		0.028		0.136		0.179		0.036	
K	0.030		0.012		0.002		0.005		0.006		0.011		0.001	
Mg#	83.73		85.67		85.85		90.30		80.19		84.70		85.63	
Ca#	11.76		7.23		10.87		5.16		17.12		18.76		9.49	

Numbers in parentheses are one standard deviation

* CO_2 content calculated by difference of 100 and the measured analytical total from EPMA

$^{\#}$ CO_2 content calculated by mass–balance calculation

^{a} Cations calculated on the basis of 8 oxygens

increasing temperature, which corresponds to an increase in pyrope component, from 90.4 to 94.5 at 10 GPa and from 91.3 to 96.1 at 20 GPa. Please note that at depth greater than 250 km, garnet can contain up to 15 mol % ferric iron in total Fe (Rohrbach et al. 2007).

Olivine polymorphs-olivines are subidiomorphic to euhedral and up to 20–100 μm long crystals (Fig. 1a, b). Olivine crystals are inclusion-free, whereas wadsleyites always contain garnet inclusions (Fig. 1d, e). The Mg# of olivine/wadsleyite increases slightly with increasing temperature. The Mg# of wadsleyite is lower (92.7–93.7) than that of olivine (94.5–94.8) in ACP. The Mg# correlates positively with the forsterite component.

Clinoenstatite-pyroxenes in the run products form tabular and 5–15 μm large grains (Fig. 1a). In ACP bulk composition, clinoenstatite is stable up to 1,700 °C at 10.0–12.5 GPa and it is stable at higher temperature (1,825 °C) at 15 GPa. Clinoenstatite has nearly pure (Mg, Fe)SiO_3 composition and contains 0.1–0.3 wt % Al_2O_3 and 0.4–0.6 wt % CaO. Cen has Mg# of 94.7–96.5 and Ca# of 0.8–1.1. In PERC bulk composition, clinopyroxene is

stable to 1,800 °C at 10–15 GPa. At 1,800 °C and 10 GPa, Cpx has Mg# of 91.8 and Ca# of 21.5 and contains 1.1 wt % Al_2O_3 and 0.8 wt % Na_2O.

Melt compositions

The melts quench to the mixtures of carbonate and silicate phases with feathery quench crystals of typically 1–3 μm across and 5–50 μm length (Fig. 1f). Melts are alkali-rich carbonated silicate melts at the pressures and temperatures targeted in this study. We assume that all CO_2 in the run products partitioned into the melt.

ACP bulk composition

At 10–20 GPa, the near-solidus initial melts are magnesio–carbonatitic in composition containing < 10 wt % SiO_2 and > 40 wt % CO_2, and 10–13 % melt fractions were produced (Ghosh et al. 2009). Carbonatitic melt has Mg# of 90.8–93.9 and Ca# of 22.8–36.6. With increasing temperature, carbonated silicate melts (> 25 wt % SiO_2, < 25 wt %
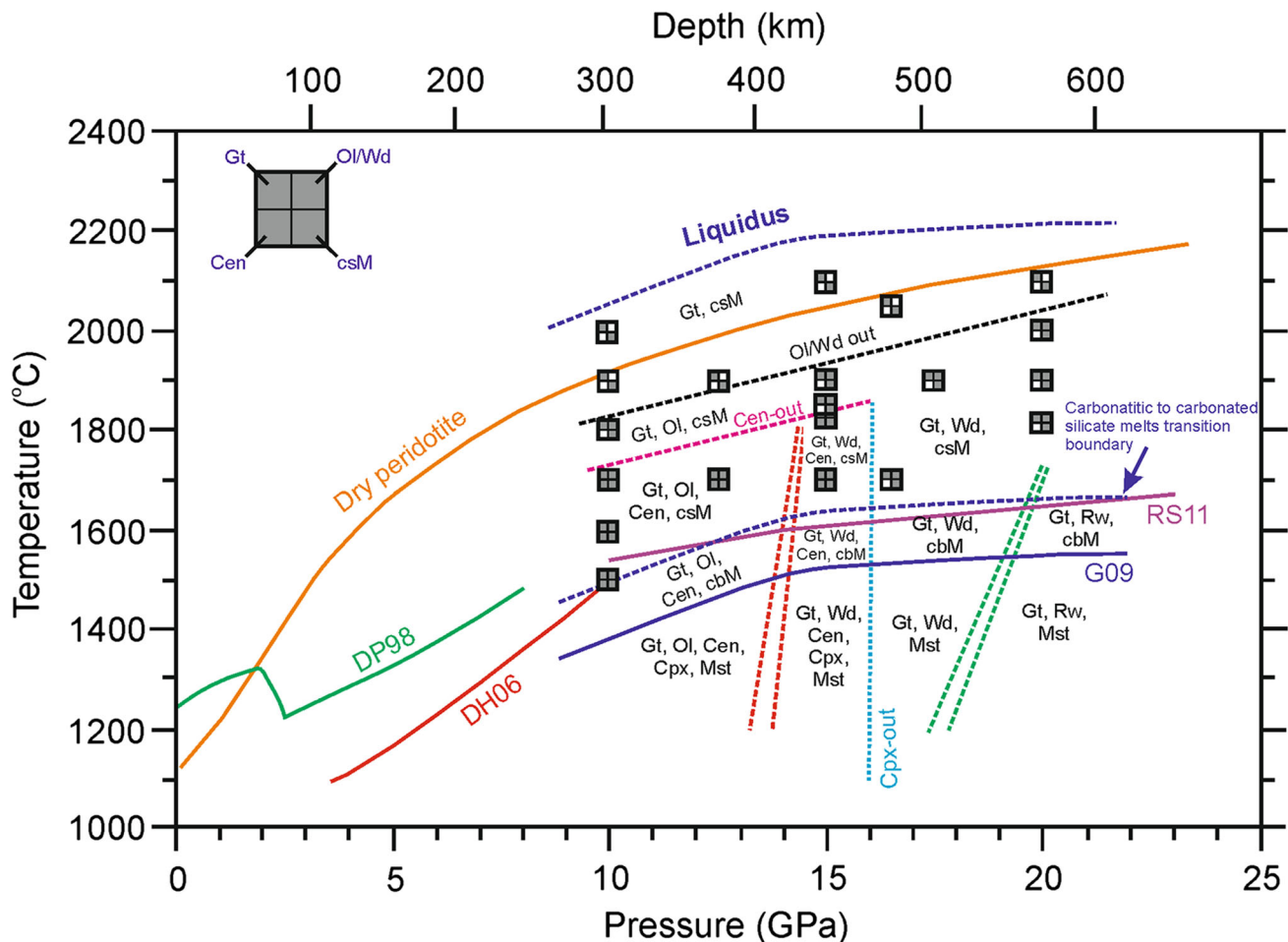
Fig. 3 Pressure–temperature diagram for melting experiments of alkali-rich carbonated peridotite (ACP) and illustrating the solidi of carbonated peridotites. *Squares*—experimental points in this study. *Filled squares* of each symbol indicate observed phases under run conditions. *Blue solid curve* (G09) is the solidus for alkali-rich peridotite (with 5 wt % CO_2) from Ghosh et al. (2009). The *dashed blue curve* near the solidus indicates the approximate boundary between carbonatite and carbonated silicate melts in ACP at 10–20 GPa. *Red curve* (DH06): solidus of fertile peridotite (with 2.51 wt % CO_2) from Dasgupta and Hirschmann (2006), *green curve* (DP98): solidus of a model CaO–MgO–Al$_2$O$_3$–SiO$_2$ (CMAS) + CO_2

from Dalton and Presnall (1998b), purple curve (RS11): solidus of fertile peridotite (with 5 wt % CO_2) from Rohrbach and Schmidt (2011), and *orange curve* is the solidus of dry peridotite (KLB-1) from Herzberg et al. (2000). *Dash red* and *green double lines* show olivine-to-wadsleyite transition from Morishima et al. (1994) and wadsleyite-to-ringwoodite transition from Suzuki et al. (2000b). *Magenta and cyan dashed lines* show the clinoenstatite-out and clinopyroxene-out boundaries. *Ol* olivine, *Wd* wadsleyite, *Rw* ringwoodite, *Cen* clinoenstatite, *Cpx* clinopyroxene, *Mst* magnesite, *csM* carbonated silicate melt, *cbM* carbonatite melt

CO_2) are produced at melt fractions from 26 to 85 % in all experiments in the present study. A transition from carbonatitic-to-carbonated silicate melts is observed from 1,400 to 1,700 °C at 10 GPa, from 1,600 to 1,825 °C at 15 GPa, and from 1,630 to 1,900 °C at 20 GPa, respectively. Although few runs show intermediate composition with 14.3–24.0 SiO$_2$ and 23.0–38.4 CO_2 from 1,600 to 1,800 °C at 10–20 GPa, SiO$_2$ contents increase from 17.8 to 40.6 wt % between 1,600 and 2,000 °C at 10 GPa, from 31.9 to 38.5 wt % between 1,825 to 2,100 °C at 15 GPa, and from 23.8 to 42.9 wt % between 1,810 and 2,100 °C at 20 GPa, respectively. With increasing temperature, MgO and Al$_2$O$_3$ contents also increase, whereas TiO$_2$, FeO$_{tot}$, and CaO

contents decrease, producing at all pressures in carbonated silicate melts at ≥ 1,700 °C. Na$_2$O and K$_2$O contents in melts decrease with increasing pressure.

At 10–20 GPa, carbonated silicate melts saturated with garnet, olivine/wadsleyite, and/or clinoenstatite yielding 10.8–25.1 wt % CO_2 content in the melts. With increasing temperature and degree of melting, CO_2 contents in the melt progressively decrease to the range of 6.4–15.4 wt % once olivine/wadsleyite is exhausted. The Mg# of the carbonated silicate melts in the range of 84.2–90.3 is lower than those of the carbonatitic melts. The Ca number (Ca# = 100 × molar Ca/[Ca + Mg + Fe^{tot}]) in carbonated silicate melt decreases with temperature from 16.1 to 6.7 between 1,700 and 2,000 °C at 10
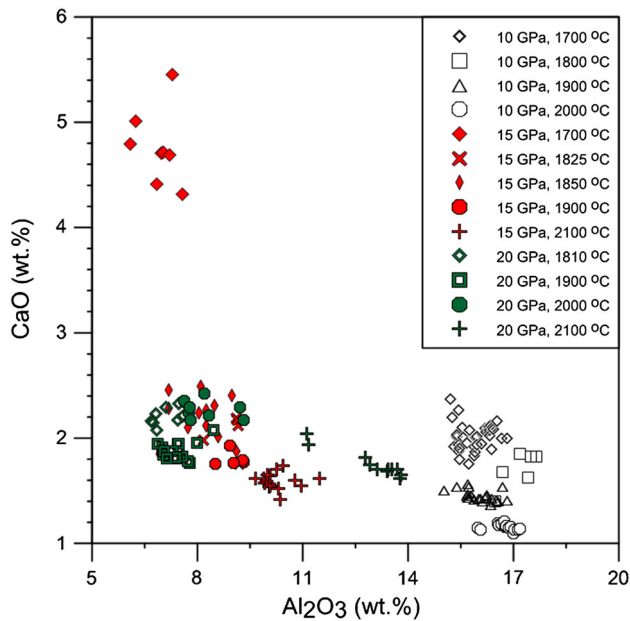
Fig. 4 Al_2O_3 versus CaO contents (wt %) in majoritic garnet at 10–20 GPa from alkali-rich carbonated peridotite (ACP). Al_2O_3 content of garnet increases with temperature at 15–20 GPa, whereas CaO content decreases with increasing temperature at 10–20 GPa

GPa, from 14.1 to 8.4 between 1,825 and 2,100 °C at 15 GPa, and from 7.2 to 5.2 between 1,900 and 2,100 °C at 20 GPa, respectively. The melt has the lowest Mg# in all experiments, and we find a general succession $Mg\#^{Cen} > Mg\#^{Oli}/Wd > Mg\#^{Gt} > Mg\#^{Melt}$ at same pressure (Tables 3, 4, 5, 6).

PERC bulk composition

At 10–20 GPa, alkali-rich and carbonated silicate melts are produced at melt fractions from 35 to 60 %. At 1,800 °C and 10 GPa, melt has a Mg# of 80.2, Ca# of 17.1, contains 37.8 wt % SiO_2, 1.6 wt % of Al_2O_3, and 12.5 wt % CO_2. At 20 GPa, SiO_2 contents increase from 24 wt % at 1,800 °C to ~ 35 wt % at 2,000 °C. Mg# shows little variation from 84.7 to 85.6 and Ca# decreases from 18.8 to 9.5 between 1,800 and 2,000 °C.

Discussion

Comparison with previous experimental studies on melting of carbonated peridotite

Experimental studies suggest that both carbonatitic and carbonated silicate melt (e.g., kimberlitic, melilititic, basaltic, picritic, and komatiitic melts) could be generated at different temperatures and melt fractions in carbonated peridotite at 3–7 GPa (e.g., Hirose 1997; Dalton and
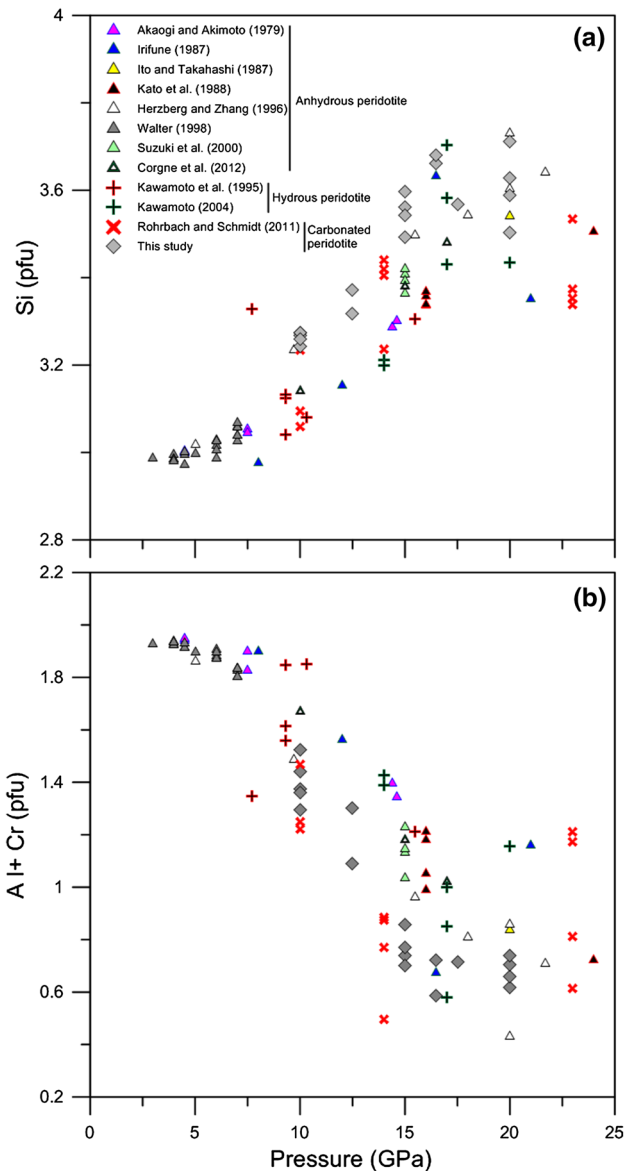
Fig. 5 a Si (pfu) and **b** Al + Cr (pfu) in garnet as a function of pressure in this study, compare with the previous experimental studies on volatile-free peridotite (Akaogi and Akimoto 1979; Irifune 1987; Ito and Takahashi 1987; Kato et al. 1988; Herzberg and Zhang 1996; Walter 1998; Suzuki et al. 2000a; Corgne et al. 2012), hydrous peridotite (Kawamoto et al. 1995; Kawamoto 2004), and carbonated peridotite (Rohrbach and Schmidt 2011)

Presnall 1998a, b; Gudfinnsson and Presnall 2005; Girnis et al. 2005; Dasgupta et al. 2007a, b; Brey et al. 2008. For the simplified system CaO–MgO–SiO_2 (CMS)–CO_2, Wyllie and Huang (1975) have first shown that at < 3 GPa, the melt will progressively change from carbonatitic to basaltic and then kimberlitic compositions with increasing temperature. Following the initial study of Wyllie and Huang (1975), Hirose (1997) studied the melting phase relations of KLB-1 peridotite with 2.6 wt % CO_2 at 3 GPa

using the diamond aggregate method and observed that near-solidus initial melt is close to carbonatite at 1,350 °C and becomes silicate-rich with increasing temperatures, close to melilitite at 1,400–1,450 °C. Then, it changes to nephelinite or tholeiite basalt at 1,475–1,525 °C. Dasgupta et al. (2007a) performed partial melting experiments on two carbonate-bearing fertile peridotites (PERC: KLB-1 + 2.5 wt % CO_2; PERC3: KLB-1 + 1.0 wt % CO_2) at 3 GPa from 1,050 to 1,600 °C. They observed a sharp transition from carbonatite-to-carbonated silicate melt and suggested that an alkaline ocean island basalt could be produced by 1–5 % partial melting of fertile peridotite source with 0.10–0.25 wt % CO_2. Continuous changes in melt compositions (without sharp transition) were observed in CMS–CO_2 at 3 GPa (Moore and Wood 1998), in CaO–MgO–Al_2O_3–SiO_2 (CMAS)-CO_2 at 3–8 GPa (Dalton and Presnall 1998b; Gudfinnsson and Presnall 2005), in KLB-1 + 5.6 wt % CO_2 at 6–10 GPa by Brey et al. (2008), and in PERC at 2–5 GPa by Dasgupta et al. (2013). In the present experiments combined with the data by Ghosh et al. (2009), we also did not observe a sharp transition from carbonatite-to-carbonated silicate melt with increasing temperature. On the other hand, the mean temperature intervals of the present study were 100 °C, which may not be sufficient to clarify a sharp transition from carbonatitic-to-carbonated silicate melt with increasing temperature and degree of melting. Previous studies (Dalton and Presnall 1998a; Gudfinnsson and Presnall 2005; Brey et al. 2008) reported melt compositions contain 10–20 wt % SiO_2 and 30–40 wt % CO_2 and show intermediate compositions between carbonatitic and carbonated silicate melts.

Our melt compositions from alkali-rich carbonated peridotite (ACP) can be directly compared with Litasov and Ohtani (2009), which describes phase relations in a model alkali-rich carbonated peridotite [NCMAS (N = Na_2O) + 5 wt % CO_2] at 10–32 GPa. Ca/(Ca + Mg) decreases from 0.18 to 0.07 between 1,700 and 2,000 °C at 10 GPa, 0.16 to 0.09 between 1,825 and 2,100 °C at 15 GPa, and from 0.08 to 0.06 between 1,810 and 2,100 °C at 20 GPa for ACP (except D007, where the CaO content is little higher, mainly due to difficulty in analyzing the small melt pockets and uncertainty is in the order of 5 wt %). At 10 GPa and 1,600 °C, melt composition in ACP shows higher Ca/(Ca + Mg), Na_2O and CO_2, and lower SiO_2, Al_2O_3, MgO, and CaO than melt from a model alkali-rich carbonated peridotite (Litasov and Ohtani 2009). This discrepancy could be explained by variations in the bulk starting materials used in these two studies. Litasov and Ohtani (2009) used a silica- and magnesia-rich bulk composition (SiO_2 = 44.8 and MgO = 41.8 wt %) compared to the bulk compositions used in the present study (Table 1), which produces < 1 % Cpx in the run

product for the former and gives lower Ca/(Ca + Mg), although CO_2 content in the bulk composition is nearly the same for both studies. Moreover, at 20 GPa and 1,800 °C, model carbonated peridotite shows higher Ca/(Ca + Mg) = 0.18 than alkali-rich carbonated peridotite (ACP, i.e., 0.08). This discrepancy could be explained by the different silicate phases coexisting with carbonated silicate melt in these two studies. At 20 GPa and 1,800 °C, Litasov and Ohtani (2009) observed garnet, wadsleyite, and $MgSiO_3$–ilmenite, coexisting with carbonated silicate melt, whereas in the present study, we found only melt coexists with garnet and wadsleyite.

Also, if we compare our melt compositions from ACP and PERC bulk compositions with recent experimental results on hydrous carbonated peridotite with high alkali and volatile contents (Brey et al. 2009, 2011; Foley et al. 2009), then melts derived from hydrous carbonated peridotites are highly alkaline and ultrapotassic silicate melts, which could form alkaline magmas (orangeites, lamproites, and aillikites).

Effect of CO_2 on melting of peridotite

Figure 6a illustrates SiO_2 versus CO_2 contents (wt %) for the melts in this study (ACP and PERC) and compares them with carbonatite and carbonated silicate melts produced in melting experiments on model and complex peridotites at 3–20 GPa (Dalton and Presnall 1998a, b; Moore and Wood 1998; Gudfinnsson and Presnall 2005; Dasgupta and Hirschmann 2007a, b; Dasgupta et al. 2007a, 2013, Brey et al. 2008). It is well known that CO_2 reduces the SiO_2 contents in the partial melts of peridotite (e.g., Eggler 1978). The CO_2 contents of carbonatite and carbonated silicate melt show negative correlation with SiO_2 and also observed by many previous studies (Dalton and Presnall 1998a; Gudfinnsson and Presnall 2005; Dasgupta et al. 2007a, 2013; Litasov and Ohtani 2009). Most compositions obtained in the present study follow a trend of decreasing SiO_2 content with increasing CO_2. At 10–20 GPa, melts are in equilibrium with olivine/wadsleyite and/or garnet. The data from the present study agree well with the previous studies defining a slope of −1 (in wt %, Fig. 6a). However, partial melts of carbonated fertile peridotites (Brey et al. 2008; Dasgupta et al. 2013) at lower pressures (4–10 GPa) plot below or above the trend, which shows lower or higher SiO_2 contents in the melts. Magnesio–carbonatitic and carbonated silicate melts show similar trends from 3 to 20 GPa, which suggests that the mixing mechanisms are similar between CO_2 and silicate melt. It is also important that the inverse relationship between SiO_2 and CO_2 in melts of carbonated peridotite does not depend strongly on temperature, pressure, and other parameters, such as the Al_2O_3, FeO, and alkali contents.
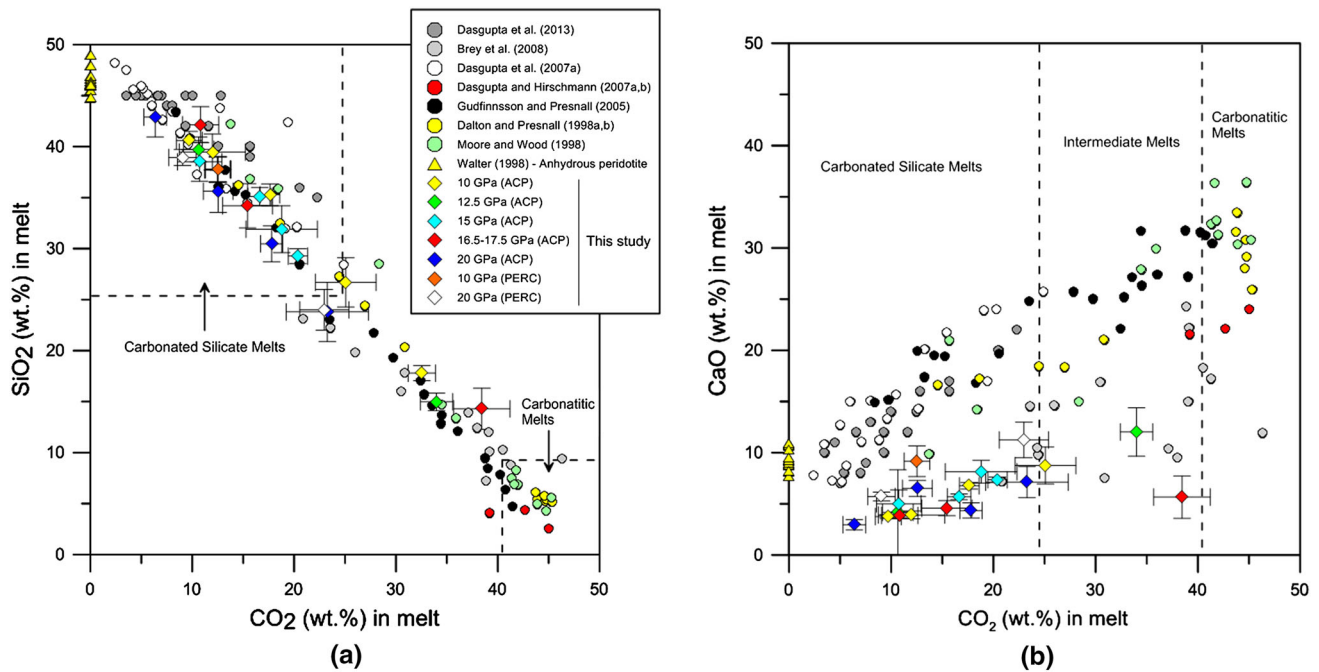
Fig. 6 **a** Measured SiO_2 content versus estimated CO_2 content. **b** Measured CaO content versus estimated CO_2 content in carbonatite and carbonated silicate melts from this study (ACP and PERC) and compared with the pervious studies in simple (Dalton and Presnall 1998a, b; Moore and Wood 1998; Gudfinnsson and Presnall 2005) and complex carbonated peridotite systems (Moore and Wood 1998; Dalton and Presnall 1998a, b; Gudfinnsson and Presnall 2005; Dasgupta and Hirschmann 2007a, b; Dasgupta et al. 2007a; Brey et al. 2008; Dasgupta et al. 2013) from 3 to 20 GPa. Data for volatile-free peridotite are from Walter (1998) at 3–8 GPa

CaO concentrations in melts increase with increasing CO_2 melt contents (Fig. 6b). The lower pressure data (3–7 GPa) show a higher trend than higher pressure data (8–20 GPa). At lower pressures, all melts coexist with olivine and orthopyroxene, whereas at higher pressure, melt mainly coexists with olivine/wadsleyite and majoritic garnet, which makes melts less calcic at lower pressure.

Mineral modes and melting reactions in carbonated peridotite between 10 and 20 GPa

By using calculated phase proportions for each experiment (Table 2; Fig. 3), we obtained the melting reactions (in wt %) for carbonated peridotite (ACP) at 10–20 GPa along the melting intervals. For PERC, the average melting reaction is unconstrained due to the large experimental interval, i.e., ∼ 200 °C.

At 10 GPa, small amount of initial carbonatitic melt (∼ 10 wt %) is generated at 1,400 °C and is controlled by melting of clinopyroxene and magnesite. The melting reaction is

$$1.40\ \text{Cpx} + 0.80\ \text{Mst} + 0.70\ \text{Ol} = 1.00\ \text{cbM} + 0.8\ \text{Cen} + 0.2\ \text{Gt} \qquad (1)$$
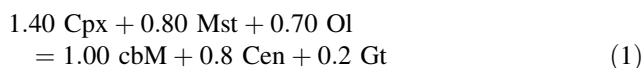
where Cpx is clinopyroxene, Mst is magnesite, Ol is olivine, Cen is clinoenstatite, Gt is garnet, and cbM is

carbonatitic melt. Further increase in temperature, large amount of carbonated silicate melt (43 wt %) is generated and clinoenstatite disappears between 1,700 and 1,800 °C. The approximate melting reaction is

$$1.02\ \text{Cen} + 0.16\ \text{Ol} = 1.00\ \text{csM} + 0.18\ \text{Gt} \qquad (2)$$
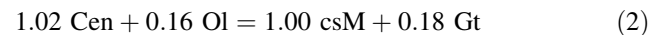
where csM is carbonated silicate melt. Carbonated silicate melts are rich in SiO_2, MgO, and CaO, and low Al_2O_3 indicating olivine and clinoenstatite is the main contributor in the melting reaction. Between 1,800 and 1,900 °C, olivine is the main contributor to melting followed by majoritic garnet resulting in 43 and 68 wt % melt, olivine is finally consumed at 1,900 °C, and garnet is stable > 2,000 °C., Melting takes place through the reaction

$$0.80\ \text{Ol} + 0.20\ \text{Gt} = 1.00\ \text{csM} \qquad (3)$$

At 15 GPa, the solidus reaction between 1,500 and 1,600 °C is

$$0.80\ \text{Cpx} + 0.80\ \text{Mst} + 0.80\ \text{Wd} = 1.00\ \text{cbM} + 1.10\ \text{Gt} + 0.30\ \text{Cen} \qquad (4)$$
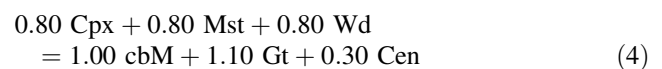
Reaction (4) is very similar to the reaction (1) at 10 GPa, consuming less clinopyroxene and producing less clinoenstatite and more garnet. To high temperature, the calculated reaction is
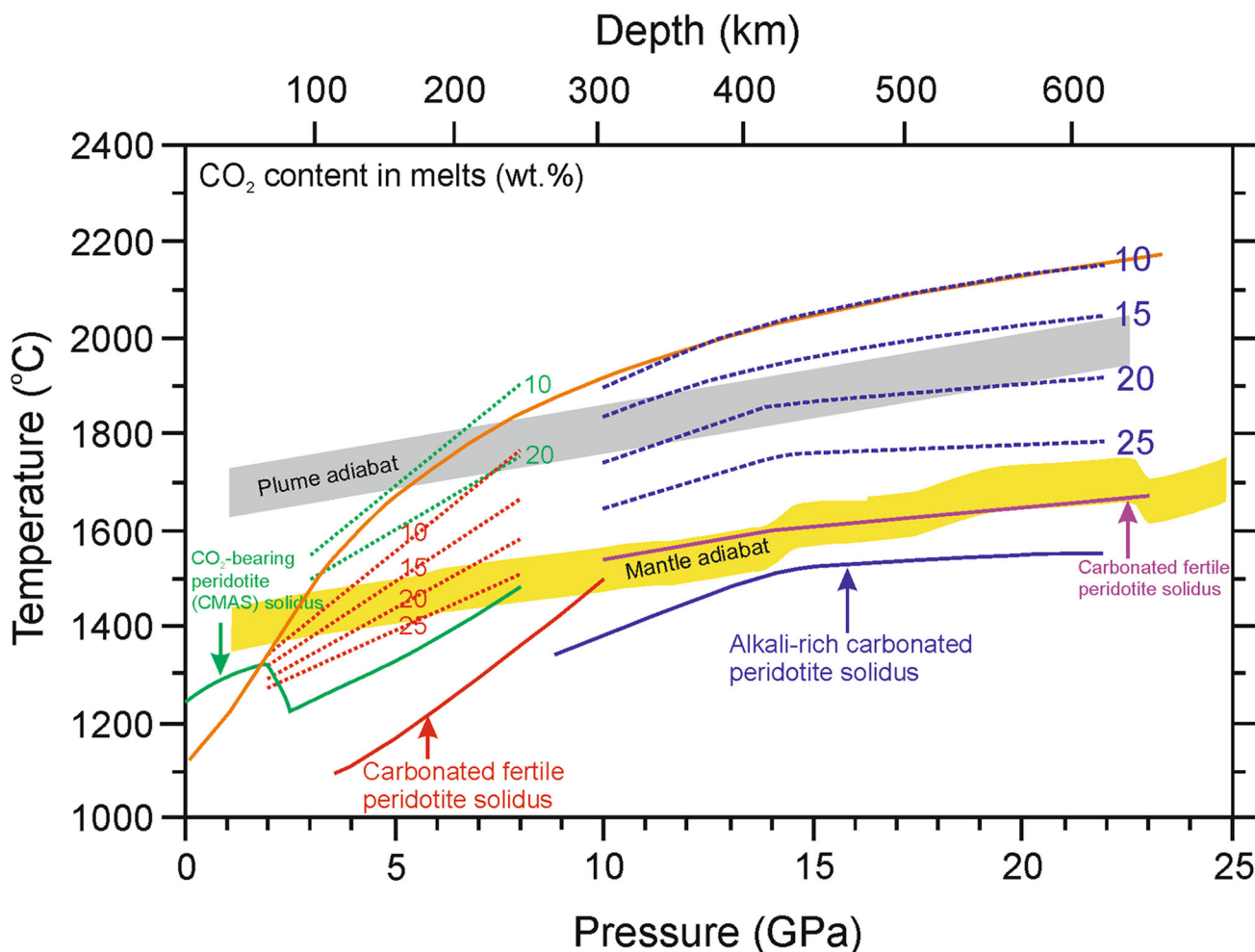
Fig. 7 Diagram shows equilibrium concentration of CO_2 in melt coexisting with peridotite phase assemblage at 10–20 GPa (this work, ACP) and compared with the previous studies on carbonated peridotite at 2–8 GPa (CMAS + CO_2: Gudfinnsson and Presnall (2005) and carbonated fertile peridotite: Dasgupta et al. 2013). *Red curve*: solidus of carbonated fertile peridotite from Dasgupta and Hirschmann (2006), *green curve*: solidus of a model carbonated peridotite from Dalton and Presnall (1998b), *purple curve*: solidus of carbonated fertile peridotite from Rohrbach and Schmidt (2011), *blue curve*: the solidus for alkali-rich carbonated peridotite from Ghosh et al. (2009), and *orange curve*: the solidus of dry peridotite (KLB-1) from Herzberg et al.(2000). *Dashed blue*, *green*, and *red lines* show CO_2 isopleths of melts for carbonated silicate melts after this study, Gudfinnsson and Presnall (2005) and Dasgupta et al. (2013), respectively. *Yellow area* shows range of potential mantle temperatures to 25 GPa considering adiabatic behavior in a convecting mantle (Stixrude and Lithgow-Bertelloni 2007). *Gray area* indicates range of plume adiabat. The *numbers* along the lines are wt % of CO_2 in the melt

$$0.45 \text{ cbM} + 0.28 \text{ Gt} + 0.15 \text{ Cen} + 0.12 \text{ Wd} = 1.00 \text{ csM} \tag{5}$$

which replacing carbonatitic melt by carbonated silicate melt. This reaction also consumes garnet, wadsleyite, and clinoenstatite. Between 1,825 and 1,850 °C, clinoenstatite is exhausted through the reaction

$$2.00 \text{ Cen} + 1.53 \text{ Wd} = 1.00 \text{ csM} + 2.53 \text{ Gt} \tag{6}$$

where Wd is wadsleyite. Finally, wadsleyite disappears between 1,900 and 2,100 °C and melt proportion increases substantially (85 wt %), and the approximate melting reaction is

$$0.53 \text{ Gt} + 0.47 \text{ Wd} = 1.00 \text{ csM} \tag{7}$$

At 20 GPa, clinopyroxene and clinoenstatite are not stable anymore. Between 1,400 and 1,600 °C, the solidus reaction is

$$1.00 \text{ Mst} + 0.27 \text{ Gt} = 1.00 \text{ cbM} + 0.27 \text{ Rw} \tag{8}$$

where Rw is ringwoodite. Further increase in temperature, the calculated melting reaction consumes carbonatitic melt + garnet + ringwoodite/wadsleyite to produce carbonated silicate melt through the reaction

$$0.57 \text{ cbM} + 0.25 \text{ Gt} + 0.18 \text{ Rw/Wd} = 1.00 \text{ csM} \tag{9}$$

Finally, wadsleyite is consumed between 2,000 and 2,100 °C, resulting 42–65 wt % carbonated silicate melt. The melting reaction is

(a)

(b)
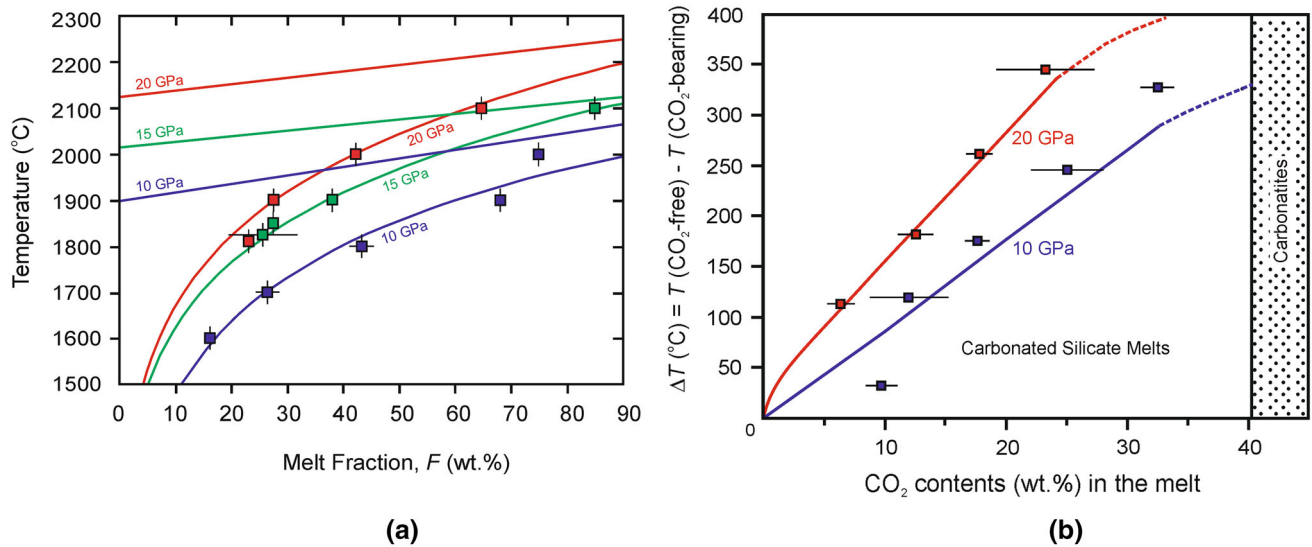
Fig. 8 **a** Temperature (*T*) versus melt fraction (*F*) data from alkali-rich carbonated peridotite (*curves*; ACP) are compared with the previous studies on volatile-free peridotite (*straight lines*; Zhang and Herzberg 1994; Herzberg and Zhang 1996; Litasov et al. 2001; Litasov and Ohtani 2002) at 10–20 GPa. For a fixed melt fraction, carbonated silicate melt stabilizes at a lower temperatures than silicate melts from a volatile-free peridotite. *Errors* are 1*σ* with respect to the mean. **b** ΔT is plotted against the CO_2 concentration in the partial melts, C_{CO2}^L. ΔT is the difference between the *T–F* trends of volatile-free and carbonated peridotite. ΔT increases from 10 to 20 GPa, which suggests CO_2 has strong effect on silicate melting. Errors are 1*σ* with respect to mean C_{CO2}^L

$$0.85 \text{ Wd} + 0.15 \text{ Gt} = 1.00 \text{ csM} \qquad (10)$$

This reaction consumes wadsleyite and garnet and produces carbonated silicate melt at 20 GPa.

Isopleths of the CO_2 contents in the melts as a function of temperature

Figure 7 compares isopleths of CO_2 in the carbonated silicate melts from the present and previous studies on carbonated peridotite (CMAS + CO_2: Gudfinnsson and Presnall 2005; PERC: Dasgupta et al. 2013; ACP: this study). Ghosh et al. (2009) determined the melts generated at the solidus are magnesio–carbonatitic melts between 10 and 20 GPa. Carbonatitic melt gradually changes to carbonated silicate melt with increasing temperature due to the dissolution of Cen, Ol/Wd, and/or Gt into the melts when *F* increases from 26 to 85 wt % at 10–20 GPa. We observed that carbonated silicate melt with 25 wt % CO_2 is stabilized at considerably lower temperature (270 °C or more) than the solidus of dry peridotite (Herzberg et al. 2000) at 10–20 GPa (Fig. 7). This suggests that carbonated peridotite melting could possibly take place at relatively lower temperatures than the volatile-free peridotite solidus at the deep upper mantle and transition zone. Dasgupta et al. (2013) constrained the location and the slope of the carbonated silicate melting from PERC at 2–5 GPa and observed that the pressure–temperature (*P–T*) slope of carbonated silicate melting is steeper than the solidus of volatile-free peridotite (Hirschmann 2000).

Isopleths of CO_2 in the silicate melts are determined previously vary considerably, mainly because of variations in the bulk starting compositions. If we compare CO_2 isopleths in model CMAS–CO_2 system at 3–8 GPa (Gudfinnsson and Presnall 2005) with carbonated fertile peridotite at 2–5 GPa (Dasgupta et al. 2013), the isopleths of CO_2 in the FeO- and Na_2O-free system are higher ($\sim$ 100 °C) than in carbonated fertile peridotite. Similar to previous studies, the concentrations of CO_2 in the melts change nearly linearly with temperature at 10–20 GPa. The SiO_2 content in the carbonated silicate melts of peridotite increases with increasing temperature from 10 to 20 GPa (18, 35 and 41 wt % SiO_2 in melt at 1,600, 1,800, and 2,000 °C at 10 GPa and 24, 36, and 43 wt % SiO_2 in melt at 1,810, 2,000, and 2,100 °C at 20 GPa). This behavior is in general agreement with the previous results at lower pressures (Moore and Wood 1998; Gudfinnsson and Presnall 2005; Dasgupta et al. 2013). The increase in SiO_2 content with increasing temperature is related to an decrease in the CO_2 solubility of the melt. Therefore, we can also plot these isopleths of CO_2 in the melts in terms of SiO_2 in the melts. If we compare ACP data with lower pressure data of PERC bulk composition at 2–5 GPa (Dasgupta et al. 2013), PERC bulk composition shows slightly lower CO_2 content, whereas model system (CMAS) reflects higher CO_2 content in the melts at lower pressures. The *P–T* slope of CO_2 isopleths in alkali-rich peridotite (ACP) is gentler than of model (CMAS) and fertile peridotite (PERC). The melt with 20 wt % CO_2 shows positive slope (i.e., $\sim$ 50 °C/GPa) for model and

fertile peridotite at 2–8 GPa (Gudfinnsson and Presnall 2005; Dasgupta et al. 2013), and these slopes are steeper than that for ACP at < 15 GPa (30 °C/GPa). Above 15 GPa, ACP shows almost flat slope with weak temperature dependence of ∼ 10 °C/GPa. This change could be explained by the different silicate phases coexisting with carbonated silicate melt between 10 and 20 GPa. Up to 15 GPa, garnet, olivine/wadsleyite, clinopyroxene, and clinoenstatite always coexist with melt, whereas above 15 GPa, garnet and olivine/wadsleyite are stable with carbonated silicate melt.

By following the approach of Dasgupta et al. (2007b), we parameterized the effect of CO_2 on melting of peridotite. To parameterize ΔT, at 10, 15, and 20 GPa, we used the following T–F trends (Fig. 8a) for volatile-free peridotite based on the results from the previous studies:

$$T(^{\circ}C) = 1{,}900.0 + 1.76 \times F(\text{wt \%}) : 10\,\text{GPa}$$

$$T(^{\circ}C) = 2{,}015.9 + 1.22 \times F(\text{wt \%}) : 15\,\text{GPa}$$

$$T(^{\circ}C) = 2{,}123.9 + 1.39 \times F(\text{wt \%}) : 20\,\text{GPa}$$

Here, we used the data of volatile-free peridotite at 10 GPa after Zhang and Herzberg (1994) and Litasov and Ohtani (2002), 15 GPa after Zhang and Herzberg (1994) and Herzberg and Zhang (1996) and at 20 GPa after Litasov et al. (2001).

To calculate the extent of silicate melting, F, induced by the amount of CO_2, we parameterized the temperature difference, ΔT, at a given melt fraction between the T–F trends for volatile-free peridotite (Zhang and Herzberg 1994; Herzberg and Zhang 1996; Litasov et al. 2001; Litasov and Ohtani 2002) and for alkali-rich carbonated peridotite (this study) as a function of the CO_2 content in the melts, C_{CO2}^{L} (wt %, Fig. 8b). The C_{CO2}^{L} versus ΔT trend is nearly linear up to ∼ 25 wt % CO_2, which is consistent with simple freezing point depression (Denbigh 1981) and can be fitted with an empirical function as:

$$\Delta T(^{\circ}C) = 9.41 \times C_{CO2}^{L} + 1586.7$$
$$\times \ln\left[\left(100 - 0.04 \times C_{CO2}^{L}\right)/100\right]$$
$$: 10\,\text{GPa} \tag{11}$$

$$\Delta T(^{\circ}C) = 7.94 \times C_{CO2}^{L} + 89.55$$
$$\times \ln\left[\left(100 + 17.1 \times C_{CO2}^{L}\right)/100\right]$$
$$: 20\,\text{GPa} \tag{12}$$

where C_{CO2}^{L} is in weight percent. We consider that CO_2 is principally incompatible in silicate phases ($D_{CO2}^{peridotite/melt} < \sim 10^{-4}$ for silicate melts and $\sim 10^{-5}$ for carbonate melts; Hauri et al. 2006; Shcheka et al. 2006), Eqs. (11) and (12) allow us to calculate the T–F trends for peridotite with variable bulk concentrations of CO_2 (Fig. 8a). Please note that Eq. (11) shows large error due to indirect determination of CO_2 contents in the melts.
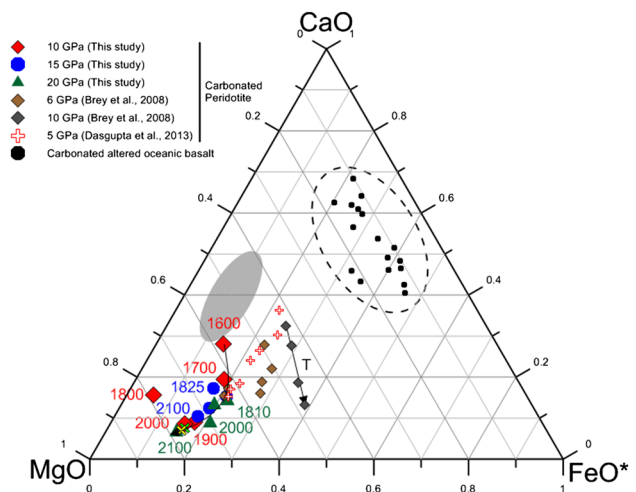
Fig. 9 Composition of carbonated silicate melts projected into CaO–MgO–FeO* (wt %) ternary from this study (*ACP* alkali-rich carbonated peridotite) and compared with experimental carbonated silicate melts produced from carbonated peridotite (Brey et al. 2008; Dasgupta et al. 2013) and the dashed area represents carbonated silicate melts produced from carbonated altered oceanic basalt (Hammouda 2003; Kiseeva et al. 2012, 2013). *Yellow* and *green crosses* show PERC and ACP bulk compositions. *Arrow* denotes evolution of carbonates silicate melts with increasing temperature. *Arrow* denotes the evolution of carbonate silicate melts with increasing temperature for Brey et al. (2008) and this study. *Gray field* shows experimental determined carbonatitic melts from carbonated fertile peridotite and alkali-rich carbonated peridotite at 6.6–20 GPa (Dasgupta and Hirschmann 2006; Ghosh et al. 2009; Rohrbach and Schmidt 2011). *Red plus sign* shows melts obtained from PERC bulk composition at 5 GPa (Dasgupta et al. 2013). Carbonated silicate melts formed from peridotites have higher Mg# and lower Ca# than those from carbonated eclogites

Figure 8a shows that the temperature difference between the T–F trends defined for volatile-free peridotite (Zhang and Herzberg 1994; Herzberg and Zhang 1996; Litasov et al. 2001; Litasov and Ohtani 2002) and carbonated peridotite (this study) between 10 and 20 GPa, which increases with increasing pressures. Therefore, CO_2 can induce and stabilize silicate melts with variable amount of CO_2 dissolved in it at relatively lower temperatures compared to volatile-free peridotite solidus at greater depths. Carbonated silicate melting begins at ∼ 400, 420, and 470 °C below the volatile-free peridotite solidus at 10, 15, and 20 GPa, respectively. This is due to the diminishing influence of non-ideal mixing between the silicates and carbonates with increasing pressure, which has been observed in the carbonated peridotite system at lower pressures (Dasgupta et al. 2007b, 2013).

Generation of peridotite-derived CO_2-rich silicate melts in the Earth's deep mantle

Figure 9 summarizes CO_2-rich silicate melt compositions generated from peridotite (Brey et al. 2008; Dasgupta et al.

2013) and altered oceanic basalt (Hammouda 2003; Kiseeva et al. 2012, 2013) in a (wt %) ternary CaO–FeO–MgO. The near-solidus melts of carbonated peridotite are carbonatitic melts with Mg# of 87-94. With increasing temperature and melt fractions, the Mg + Fe enrichment occurs mainly through melting of olivine ± clinoenstatite, which produces carbonated silicate melts. Brey et al. (2008) performed melting experiments in KLB-1 + 5.6 wt % CO_2 and suggested that a primitive kimberlite can be generated from depleted mantle peridotite that is re-enriched through volatile-bearing melts and fluids that contain high trace elements concentrations (e.g., Nb, Ta, and LREE). They also suggested that carbonated silicate melts generated from peridotite become characteristically more magnesian and less calcic with increasing degree of melting at 6–10 GPa. In ACP bulk composition, Mg# in the carbonated silicate melt increases with melt fraction and become more magnesian from 85.5 to 89.5 at 10 GPa and 83.7–90.3 at 20 GPa, respectively. Carbonated silicate melts from this study can be directly compared with Brey et al. (2008) at 6–10 GPa and Dasgupta et al. (2013) at 5 GPa. With increasing degree of melting, carbonated silicate melts show a similar trend and melts become more magnesian in carbonated peridotite. However, melts from ACP is little more magnesian than Brey et al. (2008) and Dasgupta et al. (2013) due to the relative loss of Fe from the Pt–Re capsule. Carbonated silicate melts from this study are SiO_2- and Al_2O_3-rich compared to carbonatitic melts produced by the low degree of melting of carbonated peridotite in other studies at 10–20 GPa (Ghosh et al. 2009; Rohrbach and Schmidt 2011). We attribute this change to the occurrence of relatively SiO_2-poor majoritic garnet as a liquidus phase, which increases SiO_2 content of the melts at 10–20 GPa (Table 3). The most distinguishing feature in comparison with eclogite-derived carbonated silicate melts is low Mg# and high Ca# (Hammouda 2003; Kiseeva et al. 2012, 2013). Our experiments show that carbonated peridotite can generate the CO_2-rich silicate melt that may have up to 6 wt % of alkalis (Table 2) at 10–20 GPa. It is possible that some of these high-Mg# and low Ca# melts are suitable as parental kimberlite melts (Mitchell 1995). Please note that this comparison does not cover trace element concentrations or isotopic variations. Some of these melts may originate from mantle plumes rising at the base of the transition zone or from the lower mantle (Shen et al. 1998; Li et al. 2000; Romanowicz and Gung 2002). Plumes originated in these regions may have temperatures that are 200–300 °C higher than the mantle adiabat at 660-km depth (Fig. 7; Stixrude and Lithgow-Bertelloni 2007). Some of the proposed models for kimberlite genesis favor melts originating in the transition zone or lower mantle (e.g., Ringwood et al. 1992; Torsvik et al. 2010) and from mantle plumes (e.g., Crough et al. 1980). Therefore,

carbonated silicate melting in the deep mantle does not require anomalously high temperatures and these melts may be produced over large depth intervals and in regions where redox conditions are oxidized.

The oxygen fugacity in the uppermost mantle is close to FMQ-2 (Ballhaus 1993) and decreases with increasing pressure (Woodland and Koch 2003; Stagno et al. 2013). At 10 GPa, fO_2 is close to the IW buffer and in the transition zone, fO_2 is between 2 and 0 log units below the IW buffer along the mantle adiabat (Frost and McCammon 2008). In the present study, fO_2 is significantly higher than in ambient mantle at these depths (Table 2). Consequently, carbonatitic and carbonated silicate melts from ACP and PERC lithologies can be expected to be unstable in ambient mantle (Stagno and Frost 2010) and suffer redox freezing when infiltrating the ambient mantle (Rohrbach and Schmidt 2011). However, alkali-enriched carbonatites can be produced and remobilized by carbonatitic redox melting (Foley 2011) when realms of former carbonatite infiltration are incorporated into upwelling mantle (Rohrbach and Schmidt 2011) and may thus be a possible explanation for some high electrical conductivity anomalies in the deep mantle (Shimizu et al. 2010). When carbonatitic redox melting occurs at depths less than 150 km, the ambient mantle might be sufficiently oxidized to coexist with these carbonatites (Stagno et al. 2013). Litasov et al. (2013) estimated that carbonatite diapir of 0.5–1.0 km diameter reduces its size by 30–50 % during ascent from 550 to 200 km depth. These oxidized carbonatites and, at higher degrees of melting, alkali-rich carbonated silicate melts are low in density, and viscosity can percolate upwards even through the reduced mantle via dissolution-precipitation mechanism (Hammouda and Laporte 2000; Shatskiy et al. 2013). Hydrous and carbonate-rich melts are neutrally buoyant at the top of the transition zone (Matsukage et al. 2005; Sakamaki et al. 2006; Ghosh et al. 2007). The alkali- and CO_2-rich silicate melts may react with volatile-rich materials at 410-km depth. If these refertilized domains migrate upward and convect out of the zone of metal saturation, CO_2 and H_2O flux melting can take place and kimberlite parental magmas can be generated. These mechanisms might be important for mantle dynamics and are potentially effective metasomatic processes in the deep mantle.

Conclusions

We have experimentally determined the melting phase relations and melt compositions in two carbonate-bearing peridotite compositions (ACP: alkali-rich peridotite + 5.0 wt % CO_2 and PERC: fertile peridotite + 2.5 wt % CO_2) at 10–20 GPa and 1,500–2,100 °C and constrain isopleths of the CO_2 contents in the silicate melts in the deep mantle.

- Near-solidus (ACP: 1,400–1,630 °C between 10 and 20 GPa) carbonatitic melts with < 10 wt % SiO_2 and > 40 wt % CO_2 are gradually changed to carbonated silicate melts with > 25 wt % SiO_2 and < 25 wt % CO_2 between 1,480–1,670 °C in the presence of residual majoritic garnet, olivine/wadsleyite, and clinoenstatite/clinopyroxene.

- With increasing degree of melting, the melt composition changes to an alkali- and CO_2-rich silicate melt in the composition (Mg# = 83.7–91.6; ∼ 26–36 wt % MgO; ∼ 24–43 wt % SiO_2; ∼ 4–13 wt % CaO; ∼ 0.6–3.1 wt % Na_2O; and ∼ 0.5–3.2 wt % K_2O; ∼ 6.4–38.4 wt % CO_2). The temperature of the first appearance of carbonated silicate melt at 10–20 GPa is ∼ 440–470 °C lower than the solidus of volatile-free peridotite.

- Garnet + wadsleyite + clinoenstatite + carbonatitic melt controls initial carbonated silicate melting at a pressure < 15 GPa, whereas garnet + wadsleyite/ringwoodite + carbonatitic melt dominates at pressure > 15 GPa.

- Similar to hydrous peridotite, majorite garnet is a liquidus phase in carbonated peridotites (ACP and PERC) at 10–20 GPa. The liquidus is likely to be at ∼ 2,050 °C or higher at pressures of the present study, which gives a melting interval of more than 670 °C in the carbonated systems.

- Carbonated silicate melting in the deep mantle starts at 400, 420, and 470 °C below the volatile-free peridotite solidus at 10, 15, and 20 GPa. CO_2 saturation of partial melts from carbonated peridotites shows that CO_2-rich silicate melts can be generated through partial melting of carbonated peridotite between 10 and 20 GPa, which can be in equilibrium with mantle peridotite and plays an important role in metasomatism of the deep mantle.

- Alkali-rich carbonated silicate melts may be produced through melting of carbonated peridotite to 20 GPa at near mantle adiabat or even at plume temperature. These alkali- and CO_2-rich silicate melts can percolate upwards and may react with volatile-rich materials accumulate at the top of transition zone near 410-km depth. If these refertilized domains migrate upward and convect out of the zone of metal saturation, CO_2 and H_2O flux melting can take place and kimberlite parental magmas can be generated. These mechanisms might be important for mantle dynamics and are potentially effective metasomatic processes in the deep mantle.

References

Akaogi M, Akimoto S (1979) High-pressure phase equilibria in a garnet lherzolite, with special reference to Mg^{2+}-Fe^{2+} partitioning among constituent minerals. Phys Earth Planet Inter 19(1):31–51

Ballhaus C (1993) Redox states of lithospheric and asthenospheric upper-mantle. Contrib Mineral Petrol 114:331–348

Brey G, Ryabchikov I (1994) Carbon-dioxide in strongly silica undersaturated melts and origin of kimberlite magmas. Neues Jahrbuch Fur Mineralogie-Monatshefte 10:449–463

Brey GP, Bulatov VK, Girnis AV, Lahaye Y (2008) Experimental melting of carbonated peridotite at 6–10 GPa. J Petrol 49:797–821

Brey GP, Bulatov VK, Girnis AV (2009) Influence of water and fluorine on melting of carbonated peridotite at 6 and 10 GPa. Lithos 112:249–259

Brey GP, Bulatov VK, Girnis AV (2011) Melting of K-rich carbonated peridotite at 6–10 GPa and the stability of K-phases in the upper mantle. Chem Geol 281:333–342

Canil D, Bellis AJ (2007) Ferric iron in $CaTiO_3$ perovskite as an oxygen barometer for kimberlite magmas II: applications. J Petrol 48(2):231–252

Chalapathi Rao NV, Gibson SA, Pyle DM, Dickin AP (2004) Petrogenesis of Proterozoic lamproites and kimberlites from the Cuddapah Basin and Dharwar Craton, southern India. J Petrol 45:907–948

Corgne A, Armstrong LS, Keshav S, Fei YW, McDonough WF, Minarik WG, Moreno K (2012) Trace element partitioning between majoritic garnet and silicate melt at 10–17 GPa: implications for deep mantle processes. Lithos 148:128–141

Crough ST, Morgan WJ, Hargraves RB (1980) Kimberlites: their relation to mantle hotspots. Earth Planet Sci Lett 50(1):260–274

Dalton JA, Presnall DC (1998a) The continuum of primary carbonatitic–kimberlitic melt compositions in equilibrium with lherzolite: data from the system CaO–MgO–Al_2O_3–SiO_2–CO_2 at 6 GPa. J Petrol 39(11–12):1953–1964

Dalton JA, Presnall DC (1998b) Carbonatititic melts along the solidus of model lherzolite in the system CaO–MgO–Al_2O_3–SiO_2–CO_2 from 3 to 7 GPa. Contrib Mineral Petrol 131:123–135

Dasgupta R, Hirschmann MM (2006) Deep melting in the Earth's upper mantle caused by CO_2. Nature 440:659–662

Dasgupta R, Hirschmann MM (2007a) Effect of variable carbonate concentration on the solidus of mantle peridotite. Am Mineral 92:370–379

Dasgupta R, Hirschmann MM (2007b) A modified iterative sandwich method for determination of near-solidus partial melt

compositions. II. Application to determination of near-solidus melt compositions of carbonated peridotite. Contrib Mineral Petrol 154:647–661

Dasgupta R, Hirschmann MM (2010) The deep carbon cycle and melting in Earth's interior. Earth Planet Sci Lett 298:1–13

Dasgupta R, Hirschmann MM, Smith ND (2007a) Partial melting experiments of peridotite + CO_2 at 3 GPa and genesis of alkalic ocean island basalts. J Petrol 48:2093–2124

Dasgupta R, Hirschmann MM, Smith ND (2007b) Water follows carbon: CO_2 incites deep silicate melting and dehydration beneath mid-ocean ridges. Geology 35:135–138

Dasgupta R, Mallik A, Tsuno K, Withers AC, Hirth G, Hirschmann MM (2013) Carbon-dioxide-rich silicate melt in the Earth's upper mantle. Nature 493:211–215

Dawson JB (1971) Advances in kimberlite geology. Earth Sci Rev 7:187–214

Denbigh KG (1981) The principles of chemical equilibrium: with applications in chemistry and chemical engineering. Cambridge University Press, Cambridge

Edgar AD, Charbonneau HE (1993) Melting experiments on a SiO_2-poor, CaO-rich aphanitic kimberlite from 5–10 GPa and their bearing on sources of kimberlite magmas. Am Mineral 78(1–2):132–142

Eggler DH (1978) The effect of CO_2 upon partial melting of peridotite in the system Na_2O–CaO–Al_2O_3–MgO–SiO_2–CO_2 to 35 kbar, with an analysis of melting in a peridotite-H_2O–CO_2 system. Am J Sci 278:305–343

Eggler DH, Wendlandt RF (1979) Experimental studies on the relationship between kimberlite magmas and partial melting of peridotite. Spec Publ 15:330–338

Foley S (1992) Vein-plus-wall-rock melting mechanisms in the lithosphere and the origin of potassic magmas. Lithos 28:435–453

Foley SF (2011) A reappraisal of redox melting in the Earth's mantle as a function of tectonic setting and time. J Petrol 52:1363–1391

Foley SF, Yaxley GM, Rosenthal A, Buhre S, Kiseeva ES, Rapp RP, Jacob DE (2009) The composition of near-solidus melts of peridotite in the presence of CO_2 and H_2O between 40 and 60 kbar. Lithos 112S:274–283

Forsyth DW, Scheirer DS, Webb SC, Dorman LM, Orcutt JA, Harding AJ, Blackman DK, Morgan JP, Detrick RS, Shen Y, Wolfe CJ, Canales JP, Toomey DR, Sheehan AF, Solomon SC, Wilcock WSD, Team MS (1998) Imaging the deep seismic structure beneath a mid-ocean ridge: the MELT experiment. Science 280:1215–1218

Frost DJ, McCammon CA (2008) The redox state of Earth's mantle. Annu Rev Earth Planet Sci 36:389–420

Frost DJ, Liebske C, Langenhorst F, McCammon CA, Tronnes RG, Rubie DC (2004) Experimental evidence for the existence of iron-rich metal in the Earth's lower mantle. Nature 428:409–412

Gaillard F, Malki M, Iacono-Marziano G, Pichavant M, Scaillet B (2008) Carbonatite melts and electrical conductivity in the asthenosphere. Science 322(5906):1363–1365

Gasparik T (2003) Phase diagrams for geoscientists: an atlas of the Earth's interior. Springer, New York

Ghosh S, Ohtani E, Litasov K, Suzuki A, Sakamaki T (2007) Stability of carbonated magmas at the base of the Earth's upper mantle. Geophys Res Lett 34:L22312. doi:10.1029/2007GL031349

Ghosh S, Ohtani E, Litasov KD, Terasaki H (2009) Solidus of carbonated peridotite from 10 to 20 GPa and origin of magnesiocarbonatite melt in the Earth's deep mantle. Chem Geol 262:17–28

Girnis A, Bulatov V, Brey G (2005) Transition from kimberlite to carbonatite melt under mantle parameters: an experimental study. Petrology 13(1):1–15

Gudfinnsson GH, Presnall DC (2005) Continuous gradations among primary carbonatitic, kimberlitic, melilititic, basaltic, picritic, and komatiitic melts in equilibrium with garnet lherzolite at 3–8 GPa. J Petrol 46:1645–1659

Haggerty SE (1999) A diamond trilogy: superplumes, supercontinents and supernovae. Science 285:851–860

Hammouda T (2003) High-pressure melting of carbonated eclogite and experimental constraints on carbon recycling and storage in the mantle. Earth Planet Sci Lett 214:357–368

Hammouda T, Laporte D (2000) Ultrafast mantle impregnation by carbonatite melts. Geology 28(3):283–285

Harris M, le Roex A, Class C (2004) Geochemistry of the Uintjiesberg kimberlite, South Africa: petrogenesis of an off-craton, group I, kimberlite. Lithos 74(3–4):149–165

Hauri EH, Gaetani GA, Green TH (2006) Partitioning of water during melting of the Earth's upper mantle at H_2O-undersaturated conditions. Earth Planet Sci Lett 248(3–4):715–734

Hayman PC, Kopylova MG, Kaminsky FV (2005) Lower mantle diamonds from Rio Soriso (Juina area, Mato Grosso, Brazil). Contrib Mineral Petrol 149:430–445

Herzberg C, Zhang J (1996) Melting experiments on anhydrous peridotite KLB-1: compositions of magmas in the upper mantle and transition zone. J Geophys Res 101:8271–8295

Herzberg C, Raterron P, Zhang J (2000) New experimental observations on the anhydrous solidus for peridotite KLB-1. Geochem Geophys Geosyst 1(11). doi:10.1029/2000GC000089

Hirose K (1997) Partial melt compositions of carbonated peridotite at 3 GPa and the role of CO_2 in alkali-basalt magma generation. Geophys Res Lett 24:2837–2840

Hirschmann MM (2000) Mantle solidus: experimental constraints and the effects of peridotite composition. Geochem Geophys Geosyst 1:1042

Irifune T (1987) An experimental investigation of the pyroxene-garnet transformation in a pyrolite composition and its bearing on the constitution of the mantle. Phys Earth Planet Inter 45(4):324–336

Ito E, Takahashi E (1987) Melting of peridotite at upper most lower-mantle conditions. Nature 328:514–517

Kaminsky FV, Sablukov SM, Belousova EA, Andreazza P, Tremblay M, Griffin WL (2010) Kimberlitic sources of super-deep diamonds in the Juina area, Mato Grosso State, Brazil. Lithos 114:16–29

Karato SI (2003) Mapping water content in the upper mantle. Inside the subduction factory, Washington, DC, pp 135–152

Karato S (2011) Water distribution across the mantle transition zone and its implications for global material circulation. Earth Planet Sci Lett 301:413–423

Kato T, Ringwood AE, Irifune T (1988) Experimental determination of element partitioning between silicate perovskites, garnets and liquids: constraints on early differentiation of the mantle. Earth Planet Sci Lett 89(1):123–145

Kawamoto T (2004) Hydrous phase stability and partial melt chemistry in H_2O-saturated KLB-1 peridotite up to the uppermost lower mantle conditions. Phys Earth Planet Inter 143:387–395

Kawamoto T, Leinenweber K, Hervig RL, Holloway JR (1995) Stability of hydrous minerals in H_2O-saturated KLB-1 peridotite up to 15 GPa. In: AIP conference proceedings, vol 341, p 229

Kelbert A, Schultz A, Egbert G (2009) Global electromagnetic induction constraints on transition-zone water content variations. Nature 460(7258):1003–1006

Kiseeva ES, Yaxley GM, Hermann J, Litasov KD, Rosenthal A, Kamenetsky VS (2012) An experimental study of carbonated eclogite at 3.5–5.5 GPa: implications for silicate and carbonate metasomatism in the cratonic mantle. J Petrol 53:727–759

Kiseeva ES, Litasov KD, Yaxley GM, Ohtani E, Kamenetsky VS (2013) Melting and phase relations of carbonated eclogite at 9–21 GPa and the petrogenesis of alkali-rich melts in the deep mantle. J Petrol 54(8):1555–1583. doi:10.1093/petrology/egt023

le Roex AP, Bell DR, Davis P (2003) Petrogenesis of group I kimberlites from Kimberley, South Africa: evidence from bulk-rock geochemistry. J Petrol 44:2261–2286

Li X, Kind R, Priestley K, Sobolev SV, Tilmann F, Yuan X, Weber M (2000) Mapping the Hawaiian plume conduit with converted seismic waves. Nature 405(6789):938–941

Litasov K, Ohtani E (2002) Phase relations and melt compositions in CMAS–pyrolite–H_2O system up to 25 GPa. Phys Earth Planet Inter 134:105–127

Litasov KD, Ohtani E (2009) Solidus of carbonated peridotite in the system $CaO–Al_2O_3–MgO–SiO_2–Na_2O–CO_2$ to the lower mantle depths. Phys Earth Planet Inter 177:46–58

Litasov KD, Ohtani E, Taniguchi H (2001) Melting relations of hydrous pyrolite in $CaO–MgO–Al_2O_3–SiO_2–H_2O$ system at the transition zone pressures. Geophys Res Lett 28:1303–1306

Litasov KD, Fei Y, Ohtani E, Kuribayashi T, Funakoshi K (2008) Thermal equation of state of magnesite to 32 GPa and 2073 K. Phys Earth Planet Inter 168:191–203

Litasov KD, Safonov OG, Ohtani E (2010) Origin of Cl-bearing silica-rich melt inclusions in diamonds: experimental evidence for an eclogite connection. Geology 38(12):1131–1134

Litasov KD, Shatskiy A, Ohtani E (2013) Earth's mantle melting in the presence of C–O–H–bearing fluid. In: Karato S (ed) Physics and chemistry of the deep earth. Wiley-Blackwell, New York

Marty B (2012) The origins and concentrations of water, carbon, nitrogen and noble gases on Earth. Earth Planet Sci Lett 313–314:56–66

Matsukage KN, Jing ZC, Karato S (2005) Density of hydrous silicate melt at the conditions of Earth's deep upper mantle. Nature 438(7067):488–491

Mitchell RH (1995) Kimberlites, orangeites, and related rocks. Plenum Press, New York

Moore K, Wood B (1998) The transition from carbonate to silicate melts in the $CaO–MgO–SiO_2–CO_2$ system. J Petrol 39(11–12):1943–1951

Morishima H, Kato T, Suto M, Ohtani E, Urakawa S, Utsumi W, Shimomura O, Kikegawa T (1994) The phase boundary between α and β Mg_2SiO_4 determined by in situ X-ray observation. Science 265:1202–1203

Naif S, Key K, Constable S, Evans R (2013) Melt-rich channel observed at the lithosphere-asthenosphere boundary. Nature 495(7441):356–359

O'Neill HS (1987) Quartz-fayalite-iron and quartz-fayalite-magnetite equilibria and the free energy of formation of fayalite (Fe_2SiO_4) and magnetite (Fe_3O_4). Am Mineral 72(1–2):67–75

Presnall C, Gudfinnsson GH (2005) Carbonate-rich melts in the oceanic low-velocity zone and deep mantle. Spec Pap Geol Soc Am 388:207

Ringwood AE (1975) Composition and petrology of the Earth's mantle. McGraw-Hill, New York

Ringwood AE, Kesson SE, Hibberson W, Ware N (1992) Origin of kimberlites and related magmas. Earth Planet Sci Lett 113:521–538

Rohrbach A, Schmidt MW (2011) Redox freezing and melting in the Earth's deep mantle resulting from carbon–iron redox coupling. Nature 472:209–212

Rohrbach A, Ballhaus C, Golla-Schindler U, Ulmer P, Kamenetsky VS, Kuzmin DV (2007) Metal saturation in the upper mantle. Nature 449:456–458

Rohrbach A, Ballhaus C, Ulmer P, Schindler UG, Schönbohm D (2011) Experimental evidence for a reduced metal-saturated upper mantle. J Petrol 52:717–731

Romanowicz B, Gung Y (2002) Superplumes from the core-mantle boundary to the lithosphere: implications for heat flux. Science 296(5567):513–516

Sakamaki T, Suzuki A, Ohtani E (2006) Stability of hydrous melt at the base of the Earth's upper mantle. Nature 439(7073):192–194

Sanchez-Valle C, Ghosh S, Rosa AD (2011) Sound velocities of ferromagnesian carbonates and the seismic detection of carbonates in eclogites and the mantle. Geophys Res Lett 38:L24315. doi:10.1029/2011GL049981

Schmerr N (2012) The Gutenberg discontinuity: melt at the lithosphere-asthenosphere boundary. Science 335(6075):1480–1483

Shatskiy A, Litasov KD, Borzdov YM, Katsura T, Yamazaki D, Ohtani E (2013) Silicate diffusion in alkali-carbonatite and hydrous melts at 16.5 and 24 GPa: implication for the melt transport by dissolution-precipitation in the transition zone and uppermost lower mantle. Phys Earth Planet Inter 225:1–11

Shcheka SS, Wiedenbeck M, Frost DJ, Keppler H (2006) Carbon solubility in mantle minerals. Earth Planet Sci Lett 245(3–4):730–742

Shen Y, Solomon SC, Bjarnason IT, Wolfe CJ (1998) Seismic evidence for a lower-mantle origin of the Iceland plume. Nature 395(6697):62–65

Shimizu H, Utada H, Baba K, Koyama T, Obayashi M, Fukao Y (2010) Three-dimensional imaging of electrical conductivity in the mantle transition zone beneath the North Pacific Ocean by a semi-global induction study. Phys Earth Planet Inter 183:252–269

Stagno V, Frost DJ (2010) Carbon speciation in the asthenosphere: experimental measurements of the redox conditions at which carbonate-bearing melts coexist with graphite or diamond in peridotite assemblages. Earth Planet Sci Lett 300:72–84

Stagno V, Ojwang DO, McCammon CA, Frost DJ (2013) The oxidation state of the mantle and the extraction of carbon from Earth's interior. Nature 493:84–88

Stixrude L, Lithgow-Bertelloni C (2007) Influence of phase transformations on lateral heterogeneity and dynamics in Earth's mantle. Earth Planet Sci Lett 263:45–55

Suzuki T, Akaogi M, Nakamura E (2000a) Partitioning of major elements between garnet-structured minerals and silicate melt at pressure of 3–15 GPa. Phys Earth Planet Inter 120(1–2):79–92

Suzuki A, Ohtani E, Morishima H, Kubo T, Kanbe Y, Kondo T, Okada T, Terasaki H, Kato T, Kikegawa T (2000b) In situ determination of the phase boundary between wadsleyite and ringwoodite in Mg_2SiO_4. Geophys Res Lett 27:803–806

Tainton K, McKenzie D (1994) The generation of kimberlites, lamproites, and their source rocks. J Petrol 35:787–817

Tauzin B, Debayle E, Wittingger G (2010) Seismic evidence for a global low-velocity layer within the Earth's upper mantle. Nat Geosci 3:718–721

Torsvik TH, Burke K, Steinberger B, Webb SJ, Ashwal LD (2010) Diamonds sampled by plumes from the core-mantle boundary. Nature 466(7304):352-U100. doi:10.1038/nature09216

Walter MJ (1998) Melting of garnet peridotite and the origin of komatiite and depleted lithosphere. J Petrol 39:29–60

Walter MJ, Bulanova GP, Armstrong LS, Keshav S, Blundy JD, Gudfinnsson G, Lord OT, Lennie AR, Clark SM, Smith CB, Gobbo L (2008) Primary carbonatite melt from deeply subducted oceanic crust. Nature 454:622–626

Walter MJ, Kohn SC, Araujo D, Bulanova GP, Smith CB, Gaillou E, Wang J, Steele A, Shirey SB (2011) Deep mantle cycling of oceanic crust: evidence from diamonds and their mineral inclusions. Science 334:54–57

Woodland AB, Koch M (2003) Variation in oxygen fugacity with depth in the upper mantle beneath the Kaapvaal craton, Southern Africa. Earth Planet Sci Lett 214:295–310

Wyllie PJ (1980) The origin of kimberlite. J Geophys Res 85:6902–6910

Wyllie PJ, Huang WL (1975) Influence of mantle CO_2 in the generation of carbonatites and kimberlites. Nature 257:297–299

Zhang J, Herzberg C (1994) Melting experiments on anhydrous peridotite KLB-1 from 5.0 to 22.5 GPa. J Geophy Res 99:17729–17742